Engineering Structures 359 (2026) 122677

Contents lists available at ScienceDirect

Engineering Structures

journal homepage: www.elsevier.com/locate/engstruct

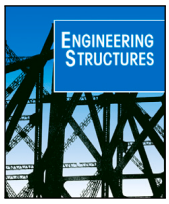

Vertical seismic isolation systems for new and existing structures in process and nuclear power plants

T. Guner *, O.S. Bursi

Department of Civil, Environmental, and Mechanical Engineering, University of Trento, Via Mesiano, 77, Trento, 38123, TN, Italy

ARTICLE INFO

Keywords:
Negative stiffness
Vertical seismic isolation
Process plants
Small modular reactor
Spherical storage tanks
Coupled Eulerian-Lagrangian analysis

ABSTRACT

This study introduces innovative vertical isolation systems, the so-called Negative-Stiffness Based Vertical ISolators (NVISs). The NVISs integrate post-tensioned cables and mechanical amplifying mechanisms to overcome buckling limitations of traditional compression-based negative stiffness isolators, offering a lightweight, tunable solution with extended negative stiffness regions. NVISs retrofitting capabilities, which do not require column cuts, facilitate practical seismic upgrades, addressing critical gaps in vertical isolation of large-scale structures. Unlike prior studies focused on small-scale applications, this work emphasises realistic applications on heavy structures. Along these lines, analytical models and dynamic analyses including friction were developed and carried out to characterise their behaviour. Small-scale experimental validation was conducted using additive manufacturing and a shake table to simulate dynamic loading conditions. Then, two realistic case studies were considered: (i) the integration of NVIS devices into the columns of a Small Modular Reactor (SMR) building; and (ii) the use of a combined horizontal–vertical isolation system composed of NVIS with horizontal rolling isolators for the protection of a spherical propylene tank in a petrochemical facility, evaluated by means of nonlinear Coupled Eulerian–Lagrangian (CEL) time-history analyses. Relevant results demonstrate more than 60% vertical seismic force reduction across diverse applications, highlighting the system's adaptability for both new and existing industrial, nuclear, and critical infrastructures.

1. Introduction

1.1. Background and motivation

Seismic protection technologies play a crucial role in safeguarding infrastructure and minimising the adverse impacts of earthquakes, particularly for critical systems such as process plant equipment, nuclear power plants (NPPs), and disaster recovery utilities. Consequently, the analysis and design of base isolation systems remain an active area of research and development. Conventional seismic isolation techniques primarily target horizontal earthquake components, effectively decoupling horizontal ground motions from the superstructure. However, these systems generally exhibit high stiffness in the vertical direction and thus provide limited protection against vertical seismic forces [1].

The vertical components of ground acceleration can be highly detrimental – especially in near-fault seismic zones – as evidenced in past events such as the 1994 Northridge, 1995 Kobe, and 2023 Kahramanmaraş earthquakes [2–4]. Strong vertical forces can compromise structural integrity by inducing yield in gravity-resisting elements, reducing load-bearing capacity, and diminishing horizontal seismic resistance. These effects pose significant risks for critical infrastructures such as nuclear plants [5] and petrochemical plants [6], where failures could have catastrophic consequences [7]. Thus, protecting industrial equipment and NPPs from vertical seismic loads remains a pressing challenge, particularly given the need to safeguard essential contents, such as flammable or refrigerating fluids.

In this study, novel vertical isolators based on negative stiffness (NS) are proposed to enhance seismic protection of industrial structures subjected to vertical loadings. The concept of NS typically involves coupling NS elements with positive stiffness components operating in parallel [8,9]. Such configurations can (i) reduce the natural frequency of the system, which is advantageous for seismic isolation; (ii) maintain a high static load-bearing capacity while achieving low dynamic stiffness, thus reducing vibration transmission; and (iii) improve stability and robustness when approaching a quasi-zero stiffness (QZS) state [10,11].

Despite promising results, the application of NS devices has been largely restricted to small-scale systems and lightweight equipment (e.g., [12,13]), with limited studies addressing large-scale vertical isolation [14,15], despite efforts dedicated to the application of NS in the control of seismic vibrations [16,17]. A recent review by Liu et al. [18]

* Corresponding author.
E-mail address: tugberk.guner@unitn.it (T. Guner).

https://doi.org/10.1016/j.engstruct.2026.122677
Received 24 November 2025; Received in revised form 9 February 2026; Accepted 4 April 2026
Available online 7 April 2026

critically examined quasi-zero stiffness (QZS) isolators, highlighting modelling inaccuracies, the neglect of friction and nonlinear damping effects, and the general limitation of QZS applications to low-mass systems.

Past research on vertical and extension to 3D isolation systems has revealed both advances and persistent challenges. Early designs employing low-shape-factor elastomeric bearings demonstrated insufficient vertical flexibility and issues related to creep and load capacity [19]. Later, sophisticated 3D systems developed in Japan – based on air springs, rolling bearings, hydraulic levelling, and cable-reinforced mechanisms – achieved effective vibration reduction, but suffered from high complexity, maintenance requirements, and costs, limiting their use in critical facilities [20,21].

Miyagawa et al. (2017) [22] developed a 3D isolator combining rubber bearings, vertical oil dampers, and disc springs. Cimellaro et al. [23] proposed 3D isolation arrangement consists of elastomeric bearings acting both in the horizontal and vertical direction where NS devices acts only in the vertical direction. Dong et al. (2025) [24] introduced a variable-stiffness and variable-damping 3D isolator. Najafijozani et al. (2020) [25] proposed six adaptive vertical isolation systems using linear and nonlinear spring–damper combinations. The effectiveness was assessed using peak isolation displacement and equipment acceleration. Other solutions – such as rubber bearings [19,26,27], air springs [28,29], mechanical spring–dampers [30–32], and hydraulic systems [33–36] – offer various benefits but remain limited in robustness. Many rely on delicate components that exhibit sensitivity to uncertainties, leading to unpredictable dynamics under extreme conditions such as major earthquakes. Moreover, current vertical isolation systems are typically more complex, larger, and heavier than their horizontal counterparts, often requiring additional mechanisms to suppress rocking motions introduced by multidirectional flexibility [5].

In contrast to the aforementioned solutions, herein we focused to offer a simpler, easy to retrofit, and potentially lower-cost alternative, making them particularly well suited for retrofitting existing industrial structures—especially those that are already isolated horizontally but remain vulnerable to vertical seismic actions. While air springs, hydraulic systems, and complex multi-component arrangements achieve multidirectional vibration reduction with high efficiency, their complexity leads to high installation/maintenance costs and often requires intricate mechanisms to be installed to control rocking motions, limiting practical adoption in industrial settings. In contrast, the proposed isolators leverages simple components, such as post-tensioned (PT) steel cables combined with mechanical amplifying mechanisms, arranged intelligently to exploit NS with hardening, enabling a highly tunable vertical isolation system. The use of PT cables allows for a lighter system free from common buckling issues.

From a regulatory point of view, both ASCE/SEI 7-16 [37] and the European standard UNI EN 15129:2018 [38] stipulate that seismic isolation systems must exhibit a stable restoring force to preserve structural integrity following an earthquake. Consequently, the use of purely NS elements – without adequate positive stiffness compensation – is prohibited due to potential instability concerns.

On the other hand, the proposed vertical isolators can be systematically designed to satisfy regulatory provisions by ensuring a stable and reliable restoring force, which is specifically addressed in this work. In particular, this stability is achieved through the coupling of NS mechanisms with positive stiffness contributions, while the use of PT steel cables provides a controlled tensile-based load path, thereby avoiding the buckling and instability issues typically associated with compression-based devices. In this way, post-earthquake stability is maintained and undesirable loss of equilibrium is prevented, preserving structural integrity under extreme vertical excitations. This unique combination of simplified configuration, retrofit practicality, code-compliant stability, and enhanced seismic performance against vertical actions clearly defines the critical research gap addressed in this study.

1.2. Scope and core contribution

In sum, to achieve the best performance of an NS device for vertical seismic isolation, this study proposes a novel Negative-stiffness-based Vertical ISolator (NVIS) that utilises the high strain capacity of PT steel cable(s) in combination with mechanical amplifying mechanisms; see Fig. 1. The proposed NVIS differs from existing solutions in the literature by a few key advantages: (i) the PT cables result in a lighter system without the common buckling issues associated with traditional compression-based QZS isolators; (ii) the involvement of mechanisms and mechanical amplifiers for the NVIS increases the NS range, delivering a highly tunable and optimizeable isolation system for vertical loads; and (iii) the NVIS devices can be applied or retrofitted to existing equipment and structures, thereby facilitating seismic upgrades of ageing industrial infrastructure.

The NVIS incorporates short elements to transfer forces from parallel-aligned straight PT cables. NVIS is designed to be suitable for large-scale structures with heavy superstructures, such as NPP buildings or large spherical tanks supported by longer columns. To validate the numerical model of the NVIS, small-scale experiments were conducted using additive manufacturing to fabricate test specimens, and a shake table was employed to simulate dynamic loading conditions.

Along these lines, the structure of the paper is as follows: Section 2 introduces the NVIS, the relevant governing static and dynamic equations; whilst the corresponding experimental validation is provided in 3. In Section 4, to support design standardisation efforts in nuclear infrastructures [39], NVIS was integrated into the NuScale Small Modular Reactor (SMR) NPP building. To demonstrate the capability of NVIS in 3D seismic isolation together with horizontal isolation solutions, Section 5 presents a case study of a spherical propylene storage tank in a petrochemical facility. A 3D seismic isolation system combining conventional rolling isolators with the NVIS was analysed using a nonlinear coupled Eulerian–Lagrangian (CEL) finite element (FE) model under multi-directional seismic excitations. Finally, Section 6 summarises the main results drawn from this investigation and includes future perspectives.

2. The negative stiffness vertical isolator "NVIS"

2.1. Conceptual overview of the NVIS

In Fig. 2, a simplified single degree-of-freedom (SDOF) spring–mass system subjected to vertical ground excitation is considered, in which a conventional positive stiffness (PS) spring is combined with an additional NS element. In traditional vertical isolators, where a soft spring is typically introduced in series to improve vibration attenuation, a fundamental trade-off exists between load-bearing capacity and isolation performance: stiff springs can sustain large static loads but provide limited low-frequency isolation, whereas soft springs enhance isolation but result in excessive static deflections and reduced stability. NS-based isolation systems aim to overcome this limitation by combining a PS component (k_{PS}) with a NS mechanism (k_{NS}), which is often achieved through geometric nonlinearity (e.g., pre-compressed structural configurations). At the equilibrium position ($x = 0$), the PS spring supports the static load, while for nonzero displacements ($x \neq 0$), the NS element generates a force in the same direction as the motion, see Fig. 2(e), effectively assisting the motion [10]. As a consequence, the overall tangent stiffness of the equivalent system is significantly reduced while static equilibrium is maintained.

Depending on the relative magnitude of the NS stiffness with respect to the PS stiffness, the equivalent stiffness k_{eq} can be reduced towards zero (Fig. 2(d)). When k_{eq} approaches zero, the system is commonly referred to as a QZS isolator. However, in practice, a perfect stiffness cancellation is not achievable due to stability constraints, nonlinear effects, and design requirements. Moreover, regulatory provisions and structural performance limits (e.g., strain demands in supporting columns)

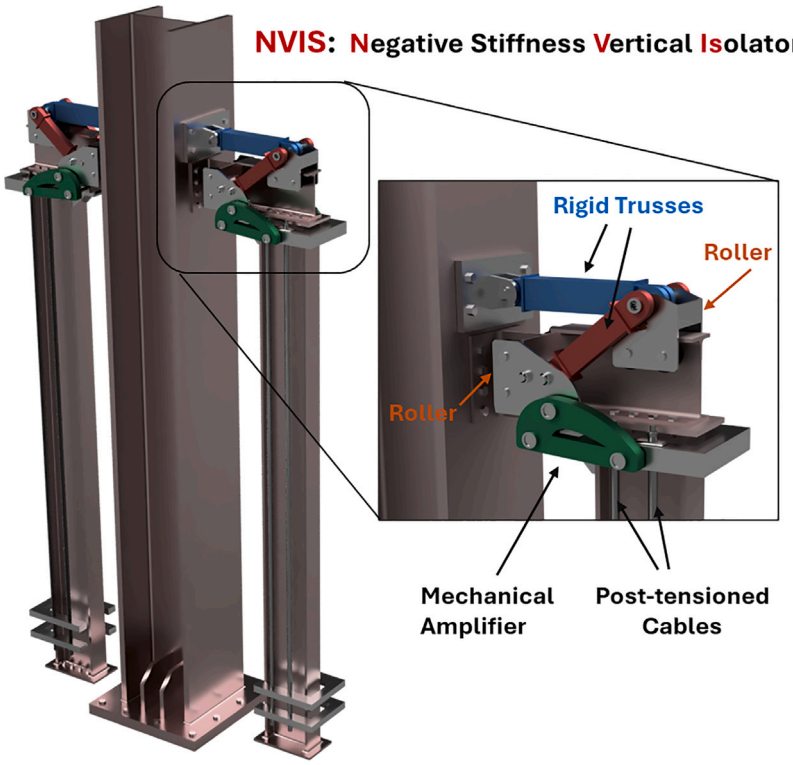

Fig. 1. Negative Stiffness Vertical Isolator.

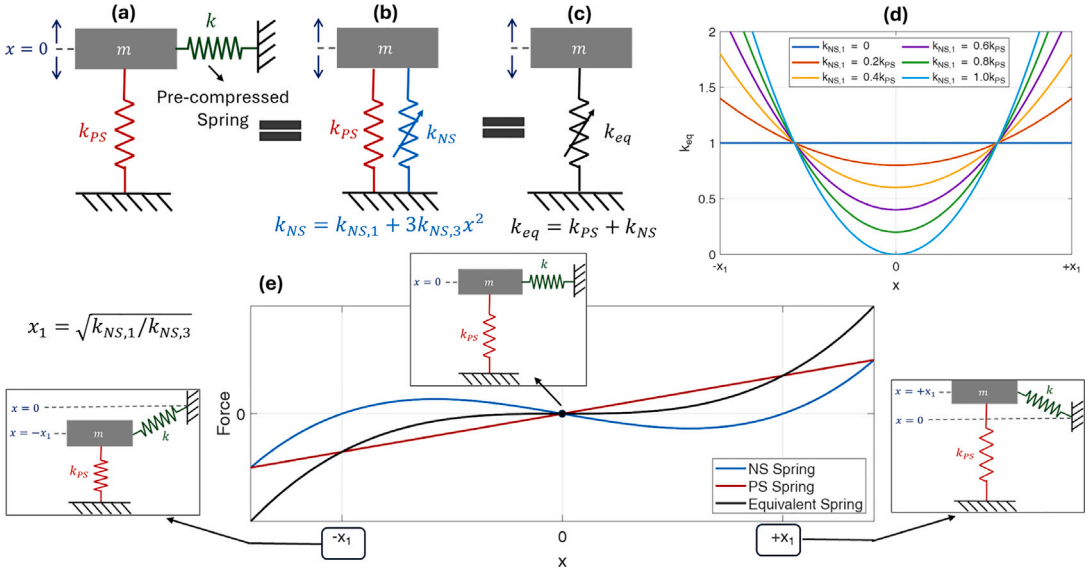

Fig. 2. Single-degree-of-freedom system combining a conventional PS spring with an additional NS element: (a) conceptual realisation of NS through a laterally attached pre-compressed spring mechanism; (b) simplified representation of the PS and NS springs connected in parallel; (c) equivalent spring–mass model with equivalent stiffness; (d) variation of the equivalent stiffness k_{eq} for different values of the NS stiffness k_{NS}; and (e) corresponding force–deformation relationships of the PS, NS, and equivalent springs, also illustrating the deformed configuration of the mechanism shown in (a).

typically prevent the realisation of a fully zero-stiffness condition in engineering applications. Therefore, in this study, the NS mechanism is employed to reduce the effective stiffness as much as possible within the boundaries of practical design limits and engineering guidelines.

Building upon this general concept, the proposed NVIS achieves a reduction in stiffness through a combination of geometric nonlinearity and pre-compressed spring elements, as depicted in Fig. 2(a). To further enhance isolation performance and improve tunability, the NVIS additionally incorporates a mechanically amplified PT cable mechanism, which generates controllable lateral compression forces and enables systematic adjustment of effective vertical stiffness. In this configuration, the NVIS does not decouple the column from the foundation; rather, it introduces additional flexibility by reducing the effective stiffness of the column (Fig. 2(d)), thereby lowering the system's natural frequency and effectively converting the column into a pseudo-isolator. Since NVIS does not require the column to be detached from the

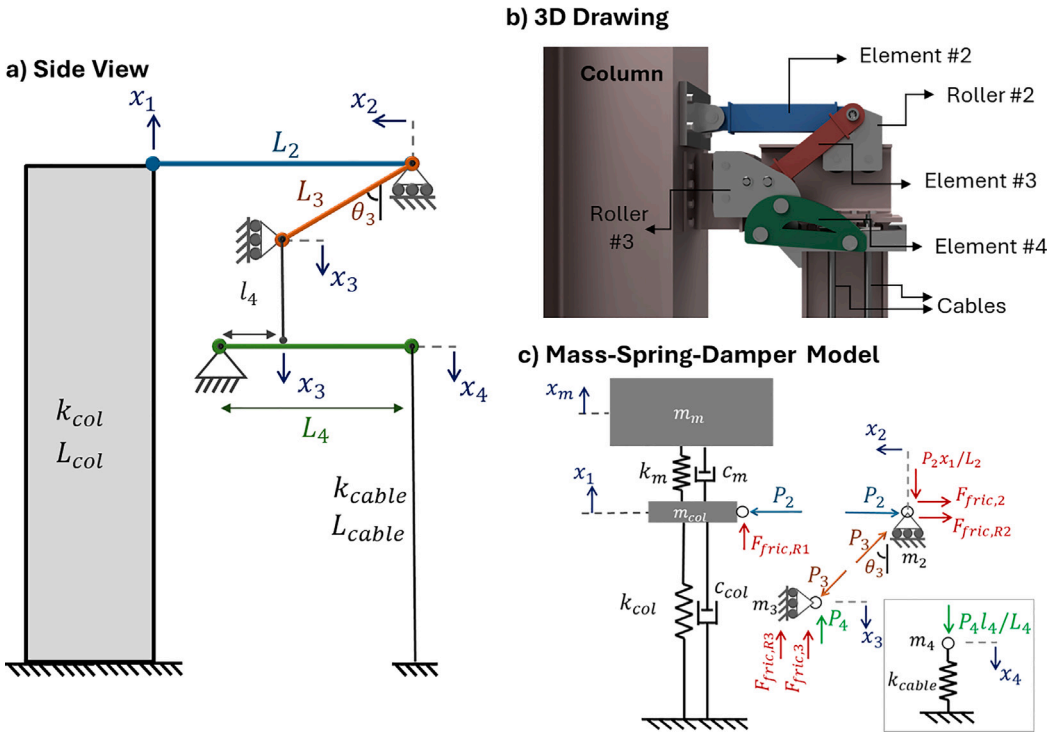

Fig. 3. Schematics of the NVIS device: (a) side view and main elements; (b) 3D view with the mechanical amplifier; (c) discretised mass–spring–damper models of the NVIS device.

foundation and can be installed in parallel with existing structural columns, it offers a retrofit-friendly solution that introduces minimal intrusion into the original system.

The schematic of the NVIS, key elements, and static/dynamical parameters are presented in Fig. 3. The proposed mechanism creates lateral compression force using a PT cable and uses short truss elements, assumed to be rigid, to transfer these forces from the column to the PT cable or vice versa.

From a physical standpoint, the NS behaviour in the proposed NVIS originates from the interaction between the PT cable and the mechanical amplifying mechanism. As vertical deformation x_1 occurs, the geometric configuration forces the PT cable to elongate through the kinematic path, generating a tensile restoring force, independent from the sign of x_1. Due to the mechanism's arrangement, this restoring force pushes top of the column along the deformation direction. This produces a negative slope in the force–displacement response, i.e., an effective NS region. In this sense, the PT cable provides a stable tensile load path, while the amplifying mechanism governs how efficiently the cable tension is converted into vertical stiffness reduction, allowing the reduced stiffness plateau to be systematically tuned through key geometric parameters.

2.2. Static equilibrium and stability

Following the notation in Fig. 3, the static equilibrium entails the following governing equation:

$$P_c L_2 - k_{col}\, x_1 L_2 + P_2\, x_1 = 0 \tag{1}$$

$$k_{cable}\, L_2\, L_4 \left(\varepsilon_{init} L_{cable} + x_3 L_4 / l_4\right) + P_3 l_4 \left(x_3 + L_3 \cos\left(\theta_3\right)\right) = 0 \tag{2}$$

$$P_2 \left(L_2 + x_2\right) + P_3 \left(x_2 + L_3 \sin\left(\theta_3\right)\right) = 0 \tag{3}$$

where k_{col} and k_{cable} are the stiffness of the column and cable elements, respectively. P_c defines the axial force on the column and x_1 is the corresponding displacement. ε_{init} define the initial cable strain. L_n and P_n are the length and axial force on the nth element. Moreover, assuming the trusses are sufficiently rigid, the geometric relations can be expressed using the Pythagorean theorem to relate the displacements of the nodes to the lengths of the truss elements:

$$\sqrt{\left(L_2^2 - x_1^2\right)} - L_2 - x_2 = 0 \tag{4}$$

$$\sqrt{\left({L_3}^2 \cos\left(\theta_3\right)^2 - 2 \sin\left(\theta_3\right)\, L_3\, x_2 - {x_2}^2\right)} - L_3 \cos\left(\theta_3\right) - x3 = 0 \tag{5}$$

$$x_4\, l_4 - x_3\, L_4 = 0 \tag{6}$$

Solving Eqs. (1)–(6) simultaneously yields,

$$\begin{aligned}&(P_c - k_{col}\, x_1)(\varphi_1 - 2L_3 cos(\theta_3)) l_4 \sqrt{L_2^2 - x_1^2} \\ &+ k_{cable} L_4\, x_1 \left(\sqrt{L_2^2 - x_1^2} - L_2 + L_3 \sin\left(\theta_3\right)\right) \\ &\times \left(\frac{L_4}{l_4}\left(L_3 \cos\left(\theta_3\right) - \varphi_1\right) - \varepsilon_{init} L_{cable}\right) = 0\end{aligned} \tag{7}$$

where:

$$\begin{aligned}\varphi_1^2 = {L_3}^2 \cos\left(\theta_3\right)^2 - \left(L_2 - \sqrt{{L_2}^2 - {x_1}^2}\right)^2 \\ + 2\, L_3 \sin\left(\theta_3\right) \left(L_2 - \sqrt{{L_2}^2 - {x_1}^2}\right)\end{aligned}$$

With regard to static stability, the equivalent system needs to satisfy the condition $k_{Eq}(x_1 = 0) \geq 0$. Thus, differentiating Eq. (7) w.r.t. x_1 and substituting $x_1 = 0$ leads to

$$k_{Eq} = \frac{dP_c}{dx_1}(x_1 = 0) = \frac{L_4\, \varepsilon_{init} L_{cable}\, k_{cable} \sin\left(\theta_3\right)}{L_2\, l_4 \cos\left(\theta_3\right)} - k_{col} = 0 \tag{8}$$

From Fig. 3 an attentive reader can deduce that the cable stiffness directly contributes to the equation with its axial stiffness. Accordingly, replacing k_{cable} with the axial stiffness yields,

$$\frac{A_{cable} E_{cable} \varepsilon_{init}}{L_{cable}} = \frac{A_{cable} \sigma_{init}}{L_{cable}} = \frac{k_{col}\, L_2\, l_4}{L_4\, L_{cable} \tan\left(\theta_3\right)} \tag{9}$$

Replacing $\sigma_{init} = \sigma_{y,cable}$, and $k_{col} = E_{col}A_{col}/L_{col}$, and $L_{cable} \approx L_{col}$ yields:

$$A_{crit,cable} = \frac{E_{col}A_{col}\,L_2\,l_4}{L_{cable}\sigma_{y,cable}\,L_4\,\tan(\theta_3)} \tag{10}$$

where $A_{crit,cable}$ is the cable area that entails a resonance frequency close to zero, and $A_{cable} > A_{crit,cable}$ results in an unstable system. $A_{crit,cable}$ therefore represents the maximum cable cross-sectional area that ensures the NVIS and column combine system stays stable, i.e. $k_{Eq} \geq 0$. As a result, the use of $A_{cable} > A_{crit,cable}$ will result in $k_{Eq} < 0$, hence an unstable system and also from practical perspective could not satisfy regulatory requirements.

As a result, L_2, l_4/L_4 and θ_3 of the truss element directly affects the required cable area. Consequently, for various L_2 and l_4/L_4 values, force–displacement and corresponding stiffness variations are presented in Fig. 4. In the rest of the Section 2, analyses were conducted for a column HD 400 × 216, $L_{col} = L_{cable} = 3$ m, $\sigma_{init} = 1000$ MPa.

In Fig. 4, the calculated values of $A_{cable} = A_{crit,cable}$ are also presented. An increase in L_2 led to an increase in $A_{crit,cable}$, which also improved the effective NS region. In scenarios where an extended quasi-zero stiffness plateau is required in respect of displacement, it is feasible to consider a larger L_2. Clearly, a larger NS plateau enables greater vertical displacement tolerance for heavy industrial equipment. From a practical design perspective this necessitates an increase in the cable's cross-sectional area, which leads to an escalation in costs, highlighting a trade-off between performance and economic feasibility. Considering reducing l_4/L_4, given in Fig. 4, reduced $A_{crit,cable}$, however, resulted in a reduced NS effective region. Although a reduced l_4/L_4 ratio is favourable for large-scale deployment, as Element #4 and hinges associated with it experiences lower forces and stresses, the effective NS performance will correspondingly decreased.

The effect of variation in θ_3 and for completeness regarding Eq. (7), the ratio L_3/L_2 provided in Fig. 5. The increase in θ_3, reduced the required $A_{crit,cable}$, but also reduced the effective region of the NS in terms of displacement, similar to L_2. In practice, θ_3 and L_2 can be tuned to optimise the trade-off between NS performance and material requirements. However, both parameters significantly influence the overall size of the NVIS, and in space-constrained applications, achievable performance may be limited. On the other hand, the L_3 effect, when considered in terms of ratio to L_2, is found to be not significant. The study demonstrated that the behaviour of NVIS can be precisely adjusted, facilitating the optimisation of vertical seismic isolation.

It is worth noting that the NVIS's effectiveness relies on the vertical displacement difference between the NVIS assembly and the connection point to the column. Conversely, see Fig. 3, the distance between the column connection and the ground is large, and to support the NVIS assembly, an additional support column is required, as depicted in Fig. 1. For completeness, the forces acting on the support column have been quantified in Appendix. Given that, under dynamic conditions, the NVIS will experience negligible inertial forces as a result of vertical seismic activities, the support columns, when designed appropriately, can be regarded as pseudo-rigid.

Furthermore, it should be noted that the formulation presented herein assumes rigid truss and mechanism elements in order to derive closed-form equilibrium and stability conditions and to clearly highlight the fundamental NS generation mechanism of the NVIS. This assumption is applicable when the stiffness of the trusses is sufficiently high compared to the forces transmitted through them, such that their elastic deformations remain negligible relative to the intended displacements. In large-scale implementations where member flexibility may become non-negligible, the compliance of the truss elements can be explicitly incorporated through refined finite-element modelling or by extending the formulation to account for member deformability. Nevertheless, the rigid-element assumption provides a valid first-order design framework for capturing the governing NS behaviour and stability limits of the proposed NVIS. In cases where deviations from the rigid-truss assumption occur, NVIS performance may be affected, which can be captured through detailed finite-element analyses. Specifically, the effective force–displacement response could be altered, potentially leading to a reduction in the width of the NS region, a decrease in the NS effect, and slight shifts in the stability margins. Nevertheless, provided that the truss members are properly designed with sufficient stiffness, the primary negative-stiffness mechanism remains operative, and these effects are expected to be minimal.

2.3. Dynamic modelling of the NVIS device

The introduction of inertial forces due to the masses of members, friction-induced forces, and inherent damping can be synthesised in the spring–damper–mass model depicted in Fig. 3(c). There, the member masses, the friction forces in the roller supports and hinged connections, and the damping associated with the main column are indicated. Thus, the system of equations of motion can be stated as:

$$\mathbf{M}\ddot{u} + \mathbf{C}\dot{u} + \mathbf{K}u + \mathbf{F}_{fric} = -\mathbf{M}i\ddot{u}_g \tag{11}$$

where $\mathbf{M}$, $\mathbf{C}$, and $\mathbf{K}$ are the mass, damping, and stiffness matrices. In particular, $\mathbf{F}_{fric}$ defines kinetic friction forces. Given the high pre-loading on the system, the static friction was neglected. This assumption is justified because the pre-tension in the cables ensures that the relative motion at the contacts is sufficient to overcome static friction even for low-amplitude excitations. Nevertheless, for extremely small inputs near the noise level or if proper treatment of the bearings and contact surfaces is lacking, stick–slip behaviour could occur. Such effects are expected to have a negligible impact compared to kinetic friction on the overall NVIS dynamic performance and can be incorporated in refined models if required for precision studies. Based on the NVIS depicted in Fig. 3(c), the system of EoMs reads:

$$m_{col}\ddot{x}_1 + c_{col}\dot{x}_1 + c_m(\dot{x}_1 - \dot{x}_m) + k_m(x_1 - x_m) + k_{col}\,x_1 + P_2\frac{x_1}{L_2} + F_{fric,R1} = -m_{col}\ddot{u}_g \tag{12}$$

$$m_2\ddot{x}_2 + P_2\frac{(L_2 + x_2)}{L_2} + P_3\frac{(L_3\,\sin(\theta_3) + x_2)}{L_3} + F_{fric,2} + F_{fric,R2} = 0 \tag{13}$$

$$m_3\ddot{x}_3 + P_3\frac{(L_3\,\cos(\theta_3) - x_3)}{L_3} + P_4L_4/l_4 + F_{fric,3} + F_{fric,R3} = -m_3\ddot{u}_g \tag{14}$$

$$m_4\ddot{x}_4 + P_4 + F_{cable} + F_{fric,R4} = -m_4\ddot{u}_g \tag{15}$$

$$m_m\ddot{x}_m + c_m(\dot{x}_m - \dot{x}_1) + k_m(x_m - x_1) = -m_m\ddot{u}_g \tag{16}$$

where F_{cable} is the force exerted on element #4 by the cables and $F_{fric,n}$ and $F_{fric,Rn}$ are the friction forces that occur on the roller supports and joints. Forces P_n are the axial force on the truss members and vary w.r.t. time. The damping constants, i.e. c_{col}, c_m were considered as modal damping with ζ_c that defines the damping ratio of the column. In detail, the friction forces read:

$$F_{fric,2} = \frac{\mu_2\,P_2\,x_1}{L_2}tanh(\dot{x}_2/v_t) \tag{17}$$

$$F_{fric,3} = \frac{\mu_3\,P_3\,(sin(\theta_3)L_3 + x_2)}{L_3}tanh(\dot{x}_2/v_t) \tag{18}$$

$$F_{fric,R1} = \mu_{r,1}P_2tanh(\dot{x}_1/v_t) \tag{19}$$

$$F_{fric,R2} = (\mu_{r,2}P_2 + \mu_{r,2}P_3)tanh(\dot{x}_2/v_t) \tag{20}$$

$$F_{fric,R3} = (\mu_{r,3}P_3 + \mu_{r,4}P_4)tanh(\dot{x}_3/v_t) \tag{21}$$

$$F_{fric,R4} = \mu_{r,4}P_4tanh(\dot{x}_4/v_t) \tag{22}$$

In particular, μ_n is the kinetic friction constant between the roller supports and the guided connection, whilst $\mu_{r,n}$ are the rotational kinetic frictions at the joints. For ease of integration, the change in direction of the friction forces was smoothed using the regularisation factor $tanh(\dot{x}_n/v_t)$, where v_t defines the kinetic friction threshold velocity.

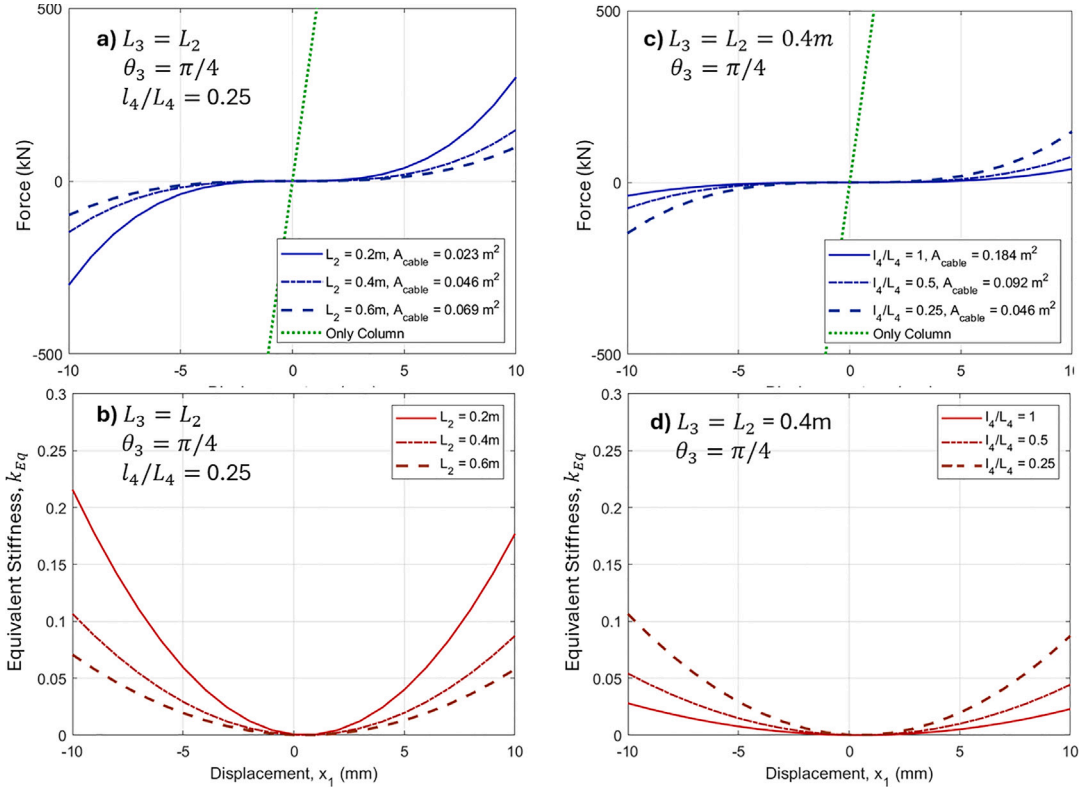

Fig. 4. Force–displacement (top row) and corresponding equivalent stiffness–displacement (bottom row) relationships for various: (a–b) L_2, and (c–d) l_4/L_4 values (Baseline values indicated on the plots and $A_{cable} = A_{crit,cable}$, $L_{col} = L_{cable} = 3$ m, $\sigma_{init} = 1000$ MPa)

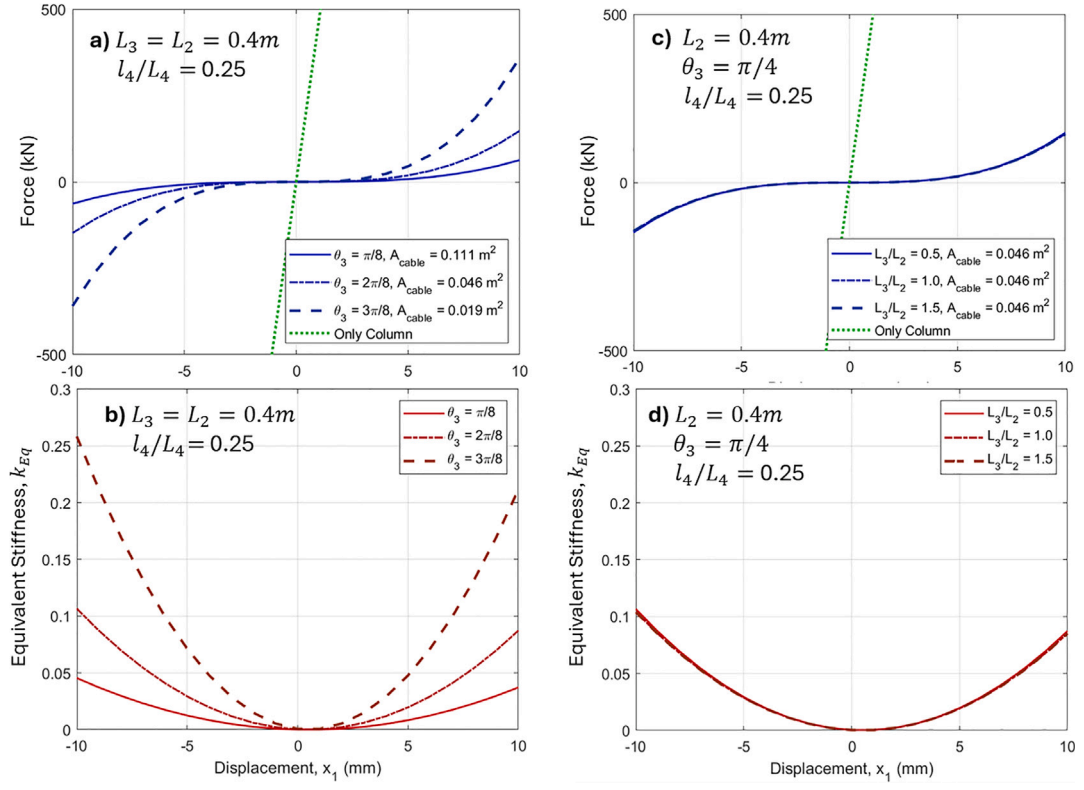

Fig. 5. Force–displacement (top row) and corresponding equivalent stiffness–displacement (bottom row) relationships for various: (a-b) θ_3, and (c-d) L_3/L_2 values (Baseline values indicated on the plots and, $A_{cable} = A_{crit,cable}$, $L_{col} = L_{cable} = 3$ m, $\sigma_{init} = 1000$ MPa)

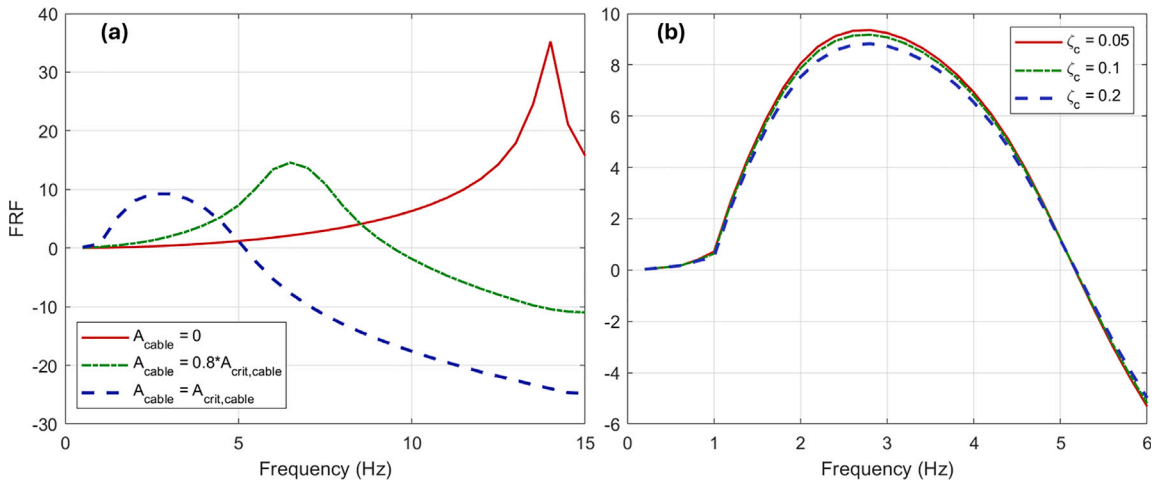

Fig. 6. FRFs of coupled systems with the NVIS: (a) influence of the A_{cable} parameter when $\zeta_c = 0.05$; and (b) the effect of the damping ratio, ζ_c when $A_{cable,crit} = A_{cable}$.($\mu_n = \mu_{r,n} = 0.2$, $A_0 = 0.1\ g$).

Then, the system of EoMs Eq. (11) was solved numerically using the ode45 solver in MATLAB [40]. For simplicity, herein, the input ground acceleration was modelled as a frequency sweep and the frequency response function (FRF):

$$FRF(f) = 20log_{10}\left(\frac{\max(\ddot{x_m})}{\max(\ddot{u_g})}\right) \tag{23}$$

was computed for the main mass acceleration $\ddot{x}_m$. Herein and after in this subsection, ($m_m = 1e5$ kg, $k_m = 5k_c$, $\zeta_m = 0.05$, $m_2 = m_3 = m_4 = 2$ kg) and ($L_2 = L_3 = 0.2$, $L_4/l_4 = 4$, $\theta_3 = \pi/4$) were considered. The influence of A_{cable} and the damping ratio ζ_c on the performance of NVIS can be obtained from Fig. 6 in terms of FRF. When A_{cable} is equal to $A_{cable,crit}$, the maximum performance can be obtained. The effect of the damping ratio ζ_c, is provided in Fig. 6(b); the reader can observe that the inherent column damping does not significantly affect the performance of NVIS.

The proposed NS isolation system is nonlinear and sensitive to the input amplitude; consequently, its effectiveness depends on the proper design and optimisation of the device for the expected working range. With reference to the input amplitude A_0, Fig. 7(a) shows the relationship between the input amplitude A_0 and the effectiveness of NS. It is evident that increasing the amplitude reduces the effective NS. However, as will be shown in Sections 4 and 5, this effect is beneficial in limiting excessive column deformations—provided that the system is properly designed. However, the results depicted in Fig. 7 show that the increased input amplitude creates a slow shift of the resonance peak to the left, due to vertical actions, also creating acceleration on the components of NVIS. Consequently, in the event of unexpected strong input, the stability of the system can be compromised. When peak displacement values are observed, NVIS reaches about a 10 mm range; however, a longer column allows for more elastic deformations, and with proper design, these axial deformation values can be tuned.

The impact of friction on the system was analysed as depicted in Fig. 8. The kinetic friction coefficients were selected based on a combination of values available online and typical properties of roller and pinned joints; specifically, the linear and rotational friction coefficients were taken as in the range of $0 \leq \mu \leq 0.4$, where maximum 0.4 coefficient was used as a representative of steel-steel dry contact without lubrication as a worst case scenario. The threshold velocity v_t was set to 0.0005 m/s, corresponding to approximately 5% of the minimum characteristic velocity observed in the system ($v \approx 0.01$ m/s) under low frequency-amplitude input, ensuring smooth transition between kinetic friction regimes. In Fig. 8, initially, an increase in the frictional coefficient of the roller support #2, denoted as μ_2, was found to exert no influence on the overall system dynamics. The varied μ_3 FRF results are depicted in Fig. 8(b). In this case, the angle $\theta_3 = pi/4$ entails high normal forces acting on roller #3, and affects the FRF response. High friction force results in unfavourable performance in the lower and higher frequency ranges, e.g. 1–2 & > 4 Hz; whilst in 2–4 Hz range, resonant peak amplitudes are reduced, as a result of dissipation. The friction forces resulting from the pinned joints were also considered and are plotted in Fig. 8(c). Rotational friction forces result in FRF increases, whilst shifting the resonance frequency to the left, can also compromise system stability if A_{cable} selected too high. In addition, parametric consideration of uncertainties in the friction coefficients within the practical range ($0 \leq \mu \leq 0.4$) indicates that while variations can slightly alter the NS effectiveness and, in cases of high friction, may compromise stability, the overall NVIS dynamic behaviour and stability margins remain largely robust. A small safety factor can be introduced in A_{cable} when excessive friction uncertainty is expected, further enhancing NVIS robustness. As illustrated in Fig. 8, the performance is not highly sensitive to moderate deviations in friction parameters, reinforcing confidence in the proposed design under realistic variability in contact conditions.

As highlighted, in practice, friction affects the frequency-dependent behaviour of the NVIS. High friction can reduce peak amplitudes in certain frequency ranges due to energy dissipation, but may also degrade performance at other frequencies or shift resonance, potentially limiting the effective NS displacement range. Therefore, in large-scale applications, friction should be considered during the design and tuning of NVIS devices and minimised through the use of appropriate bearings, as it influences both isolation efficiency and overall system stability, particularly under large vertical loads. Moreover, when friction is kept under control, NVIS design can be simplified by relying primarily on static analyses, thereby reducing overall design complexity.

3. Experimental validation

To validate the numerical model of the NVIS device, a small-scale experimental test was conducted. The experimental setup was designed to assess the dynamic response of the system under controlled loading conditions and to verify the accuracy of the governing equations and model predictions presented in Section 2. The test specimen were fabricated using the additive manufacturing Fused Filament Fabrication technique, allowing for the reproduction of the components of the NVIS in small scale and details of the experimental setup is given in Fig. 9.

Dynamic excitation was introduced using a small-scale shake table, as shown in Fig. 9(d). The shake table can provide input profiles with a maximum velocity of 0.5 m/s, as a result higher mass and flexible column had to be used. The specimen was mounted horizontally on the

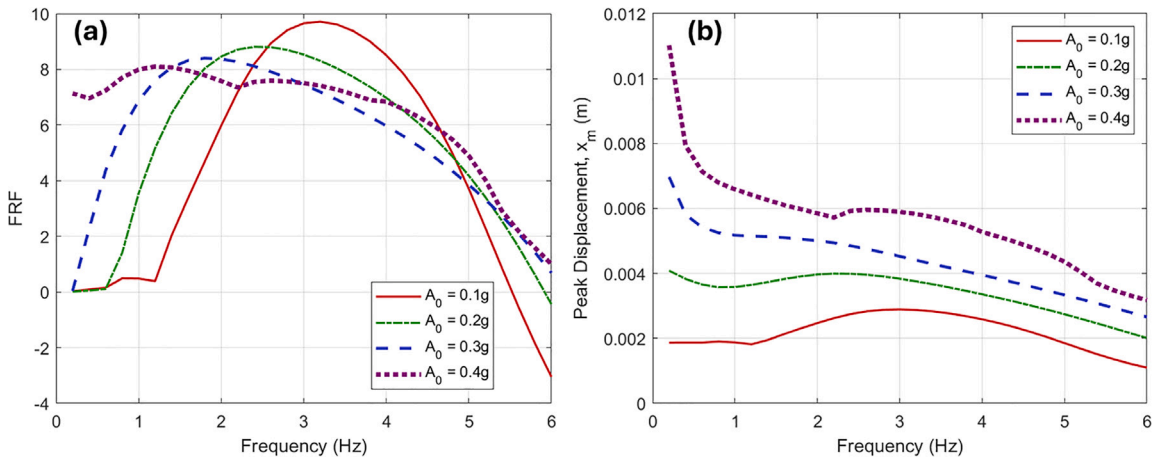

Fig. 7. Influence of input amplitude A_0 on the performance: (a) FRF results; (b) Peak displacement of the main mass ($A_{cable} = A_{cable,crit}$, $\mu_n = \mu_{r,n} = 0.2$)

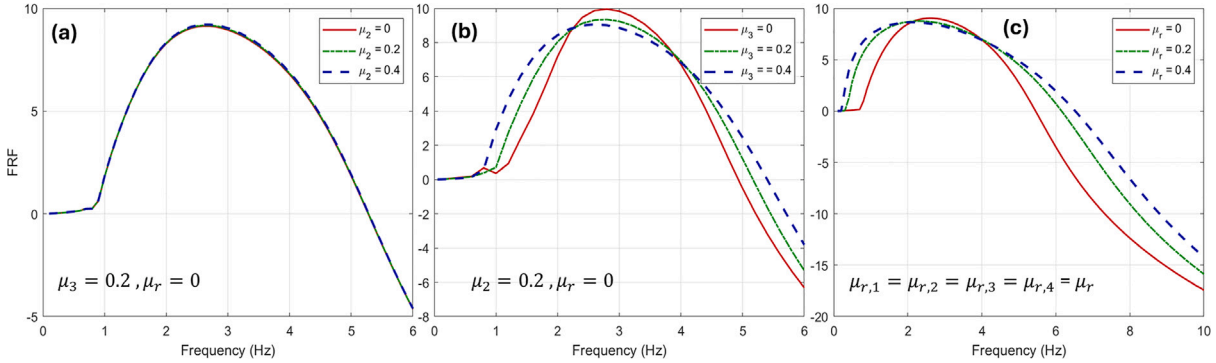

Fig. 8. Influence of (a) friction on the roller Support #2, i.e. μ_2, (b) friction on the roller Support #3, i.e. μ_3, and (c) friction forces resulting from pinned joints, i.e. $\mu_r = \mu_{r,1} = \mu_{r,2} = \mu_{r,3} = \mu_{r,4}$, on frequency response functions results ($A_{cable} = 0.95A_{cable,crit}$, $A_0 = 0.1$ g)

shake table, while the boundary conditions were maintained consistent with those assumed in the numerical model. The shake table was employed to apply 100-second frequency sweeps over the relevant frequency range, i.e. f_s = 5–20 Hz, for the purpose of validating the numerical analysis results. This frequency range also coincides with the vertical natural frequencies of heavy industrial equipment and structures. For example, the SMR building studied in Section 4 has a vertical resonance frequency of approximately 16 Hz, which lies within the tested range, ensuring that the small-scale experiments capture the relevant dynamic behaviour.

The designed column with the attached mass, whose details are presented in Fig. 9(a), corresponded to a natural frequency of ω_n = 14.85 Hz (E_{TPU} = 30 MPa). The designed NVIS device entails m_2 = m_3 = m_4 = 10 g, L_2 = L_3 = 34 mm, L_4/l_4 = 4, θ_3 = 42°, μ_n = $\mu_{r,n}$ = 0.2, and A_{cable} = 78.5 mm^2. The friction coefficient was assumed as an average value of $\mu = 0.2$, resulting from the small bearings in the setup; moreover, in accordance with Section 2.3 moderate variations in μ have a negligible influence on the overall dynamic response, and therefore this nominal value was adopted in the simulations. Using the case without NVIS attached, the damping in the column was identified as ζ_c = 0.1 and linear bearing friction was considered as (μ = 0.05). The response data were collected using a ±50 mm LVDT displacement sensor; see Fig. 9(d), with an accuracy of 0.01 mm, a sampling frequency of 800 Hz, and uncertainty ±0.2 mm based on manufacturer linearity specification. The time-domain signals were analysed using MATLAB's Fast Fourier Transform (FFT) to obtain the frequency-domain response. The frequency resolution was determined by the sampling frequency and the number of FFT points, enabling accurate identification of resonance frequencies and comparison with the numerical model predictions. The comparison with the corresponding numerical predictions is given in Fig. 10, together with the comparison of experimental time histories for the system without and with the NVIS, highlighting the reduction in peak response frequency and altered dynamic behaviour. To visualise the effect of instrument uncertainty in the frequency domain, a synthetic ensemble of signals was generated by adding Gaussian noise to the measured time history. The noise was drawn from a normal distribution with zero mean and standard deviation $\sigma = 0.2/2$, such that $\pm 2\sigma$ corresponds to the instrument uncertainty. FFTs were computed for all synthetic signals, and the resulting amplitude spectra were used to define a shaded error band around the FFT of the original measurement.

Overall, the experimental results exhibited good agreement with the numerical model, successfully reproducing the NS effect of the NVIS. With the NVIS attached, the fundamental natural frequency of the column was measured to be 9.75 Hz. As expected, increasing the initial cable pretension or incorporating additional cables would further reduce the effective stiffness of the system. In general, the deviations were attributed to manufacturing tolerances, frictional interactions between components, localised structural deformations, and plastic creep. These findings substantiate the validation of the NVIS model for predictive analyses and demonstrate the potential efficacy of NVIS in vibration isolation applications.

The mechanical principles of the small-scale prototype can be directly scaled up by first adjusting material properties and then proportionally scaling the dimensions of the elements to maintain similar stiffness ratios and dynamic behaviour. While the small-scale tests provide qualitative validation of the numerical model, limitations such as differences in material properties between 3D-printed polymers and structural steels, simplified friction representation, and potential localised deformations must be acknowledged. An important advantage

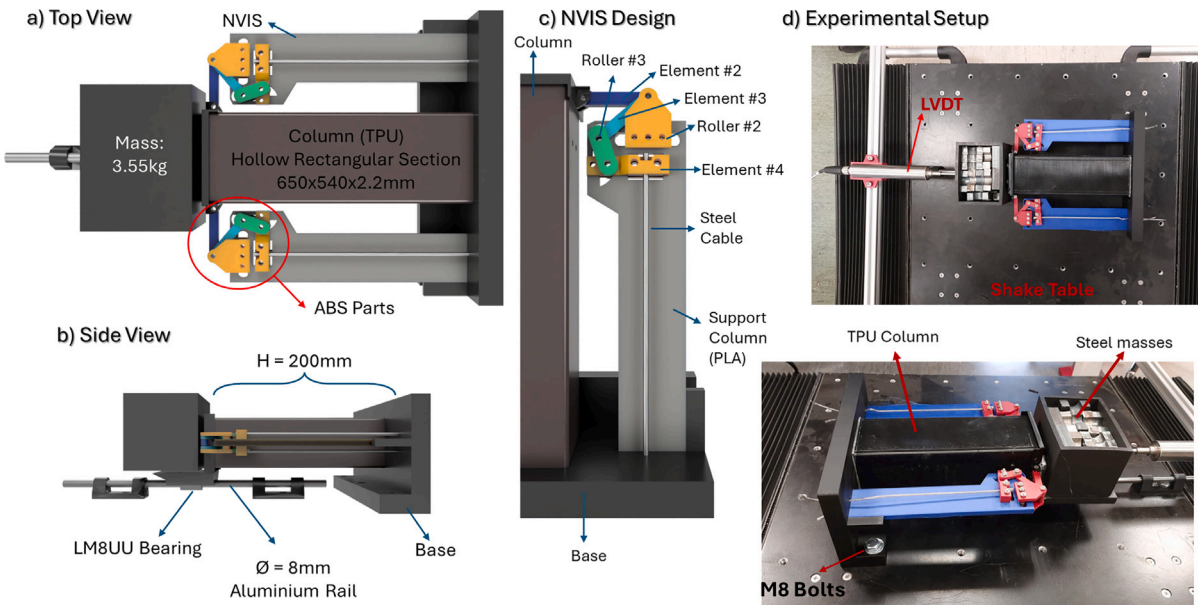

Fig. 9. Experimental setup: (a) Top view of the prototype and associated details; (b) Side view; (c) schematic design of the NVIS prototype; and (d) images of the experimental setup and the shake table.

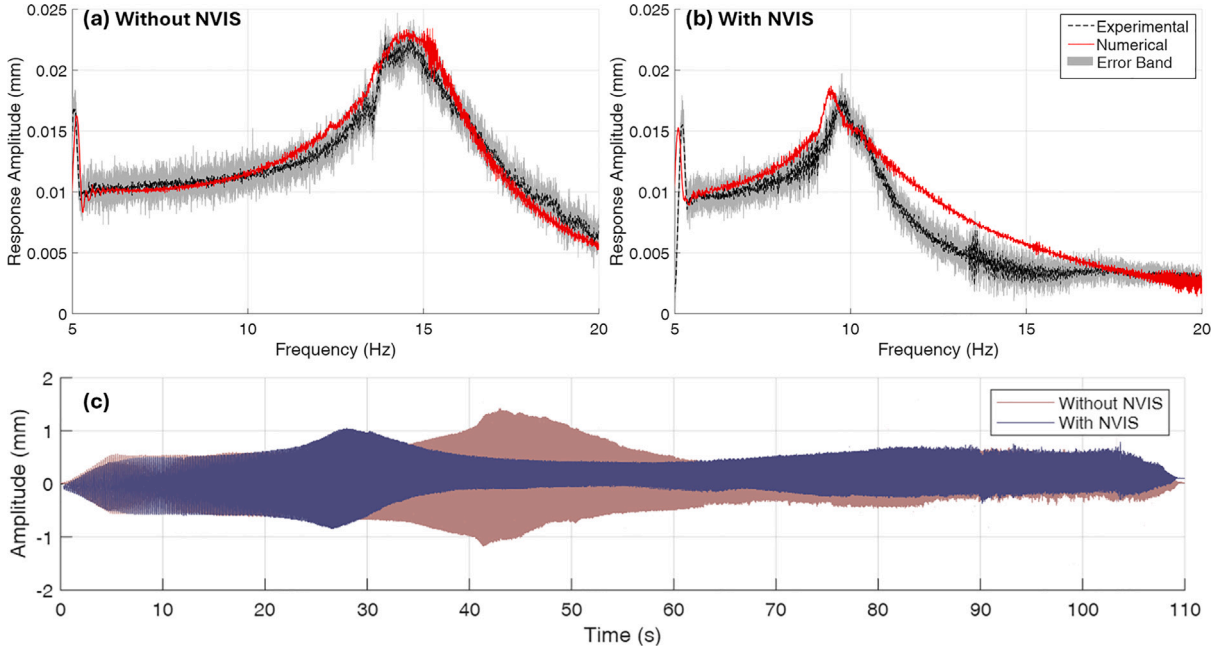

Fig. 10. Comparison between experimental measurements and numerical simulations for (a) the configuration without NVIS, (b) the configuration with NVIS attached, and (c) the comparison of experimental time history results with and without NVIS attached (Shaded grey area represents the instrument uncertainty of the LVDT.).

in large-scale applications is the use of steel or other high-strength materials, as plastics at small scale tend to exhibit localised deformations and shortened effective service life. The use of steel PT cables and mechanical amplifiers ensures that the NVIS concept can accommodate larger masses and structural loads, as the working principle is fundamentally scale-independent. Nevertheless, potential challenges in full-scale implementation, including material nonlinearity, manufacturing tolerances, and frictional effects, need to be addressed through careful selection of industrial-grade materials, precision fabrication, and proper design to ensure accurate prediction of dynamic performance and system stability.

4. Foundations of small reactor buildings endowed with NVIS devices

The first case study that has been selected for the use of NVIS devices is the main reactor building of the NuScale VOYGR-12 SMR building. It has been chosen because of its high sensitivity to vertical seismic excitations and the strict design standards imposed on NPPs [39]. In fact, significant challenges arise from: (i) the compact architecture of the SMR, which leads to high structural resonance frequencies; and (ii) the rocking behaviour due to structure asymmetry.

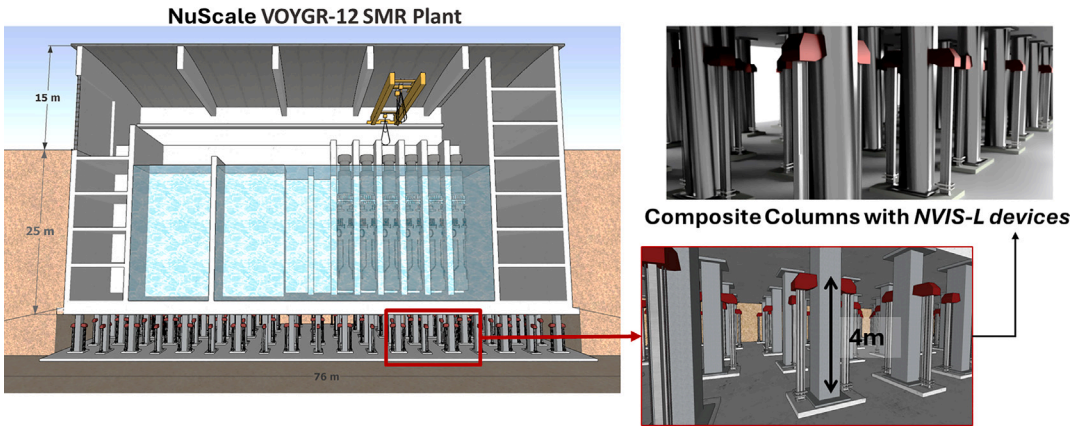

Fig. 11. Details of the NuScale VOYGR-12 SMR Building and relevant dimensions. Close-up view (right) of the foundation columns equipped with NVIS devices.

These factors, in turn, increase the likelihood of hazardous vibrations, including in the vertical direction, affecting critical components, such as reactor modules, cooling systems, and control mechanisms. Although conventional seismic isolation techniques are mainly geared towards mitigating horizontal ground motions, vertical excitations can be equally – if not more – detrimental due to the potential amplification of vertical loads on sensitive equipment [41].

Next-generation SMR buildings are engineered to enhance the safety and resilience of nuclear facilities, a goal underscored by lessons learnt from the Fukushima disaster [42]. Isolation for vertical loads will be integrated into the SMR designs to improve seismic performance, whilst simultaneously supporting design standardisation. Unlike traditional NPPs, SMRs adhere to a standardised, modular design that facilitates efficient manufacturing, transport, and deployment across various locations [43]. Although standardisation improves scalability and cost-effectiveness, it also limits the range of suitable construction sites. Therefore, integrating effective and adaptable seismic protection solutions is essential to enable the deployment of standard SMR designs at sites facing seismic hazards beyond their original design parameters [39].

The considered VOYGR-12 SMR structure integrates 12 NuScale light-water SMR power modules, with a total output of 924 MWe [44], as shown in Fig. 11. Each module, approx. 23 m tall and 4.5 m wide and is immersed in water cooling pools. The pools and SMR modules were modelled with separate DoFs, as being linked to the main SMR building frame. The considered structure has an estimated mass of120,000 tons, and with a fundamental vertical resonance frequency of about 16 Hz. The standardised design of the building represented a vertical PGA_V = 0.2 g, which was in accordance with the design basis of the earthquake (DBE) conditions. More details can be found in Guner et al. [45].

To implement vertical seismic protection, the SMR structure was positioned on a foundation system consisting of 240 composite columns, each 4 m in height. It is worth noting that such a configuration is also commonly employed for the installation of horizontal isolators in NPPs, as it facilitates both isolators and ease of maintenance. For the purpose of streamlining the narrative, horizontal isolation and actions on the SMR were excluded. Nonetheless, the subsequent section will introduce the application of NVISs in conjunction with horizontal isolation, thereby presenting a comprehensive three-dimensional isolation system. This configuration resulted in a coupled system vertical frequency of 11.4 Hz. These columns featured hollow square steel sections filled with RC, aiming at a fire resistance rating of R180 in agreement with Eurocode 1994-1-2 [46]. A steel reinforcement ratio of 6% and a concrete grade of C50/60 were adopted [47–49]. The dimensions of the designed column are 760 mm in width and 30 mm in wall thickness. The details of the SMR building with installed NVIS devices are presented in Fig. 11.

The ratio $A_{\text{cable}}/A_{\text{cable,crit}}$ for the NVIS system was determined on the basis of the peak allowable column strain. As discussed in Section 2.2, when the ratio $A_{\text{cable}}/A_{\text{cable,crit}}$ approaches unity, the effective stiffness of the coupled system reduces to zero. In this situation, see, for instance, Fig. 7(b), the NVIS devices induce significant displacements in the columns, potentially resulting in column yielding. To mitigate this effect, a design procedure is used to estimate the $A_{\text{cable}}/A_{\text{cable,crit}}$ ratio, which is subsequently verified through THAs.

The composite columns exhibit a limit-critical strain due to the yield of the HSS (S355), which occurs at $\varepsilon_y = 0.17\%$. Therefore, the corresponding nonlinear force–deformation responses of a single composite column for various $A_{\text{cable}}/A_{\text{cable,crit}}$ ratios are presented in Fig. 12(a). One can observe that the presence of NVIS devices introduces a marked nonlinearity in the force–deformation behaviour.

Given the safety requirements of the SMR, an allowable strain limit of 0.0015 was adopted. Within this range, the column stiffness was linearised and the response spectrum analysis (RSA) method was employed to estimate axial displacements. The resulting responses were then combined using the Complete Quadratic Combination (CQC) method [50]. Fig. 12(b) shows the resulting axial strains in the columns and the first vertical modal frequency of the tank with NVIS devices for different $A_{\text{cable}}/A_{\text{cable,crit}}$ ratios. These results indicate that the value of $A_{\text{cable}}/A_{\text{cable,crit}} = 1$ is not admissible. Based on the limiting column strain value of 0.15%, the corresponding ratio was determined to be $A_{\text{cable}}/A_{\text{cable,crit}} = 0.982$. This selection yielded on the elastic spectrum, i.e. the design spectrum, a coupled system vertical frequency of 3.6 Hz, which led to an approximate 48% reduction in spectral acceleration, as illustrated in Fig. 13. Clearly, this ratio is based on the site-specific design spectrum and vertical seismic hazard considered for the analysed SMR configuration. This ensures sufficient NS performance while maintaining system stability under the expected seismic loads. For other SMR installations or locations with different seismic hazard levels, this ratio should be adjusted accordingly, reflecting local site effects and the target vertical response of the structure.

Consequently, the design workflow for selecting the ratio $A_{\text{cable}}/A_{\text{cable,crit}}$ may be summarised as follows:

i. Define the allowable peak column strain, ε_y based on material and safety requirements.
ii. Compute the nonlinear force–deformation response of the composite column for a range of $A_{\text{cable}}/A_{\text{cable,crit}}$ ratios.
iii. Within the allowable strain limit $\pm\varepsilon_y$, linearise the column stiffness.
iv. Estimate axial displacement and strain demand ε_c in the column using the RSA method.
v. Identify the maximum admissible ratio $A_{\text{cable}}/A_{\text{cable,crit}}$ that satisfies the strain limit $\varepsilon_c \leq \varepsilon_y$.

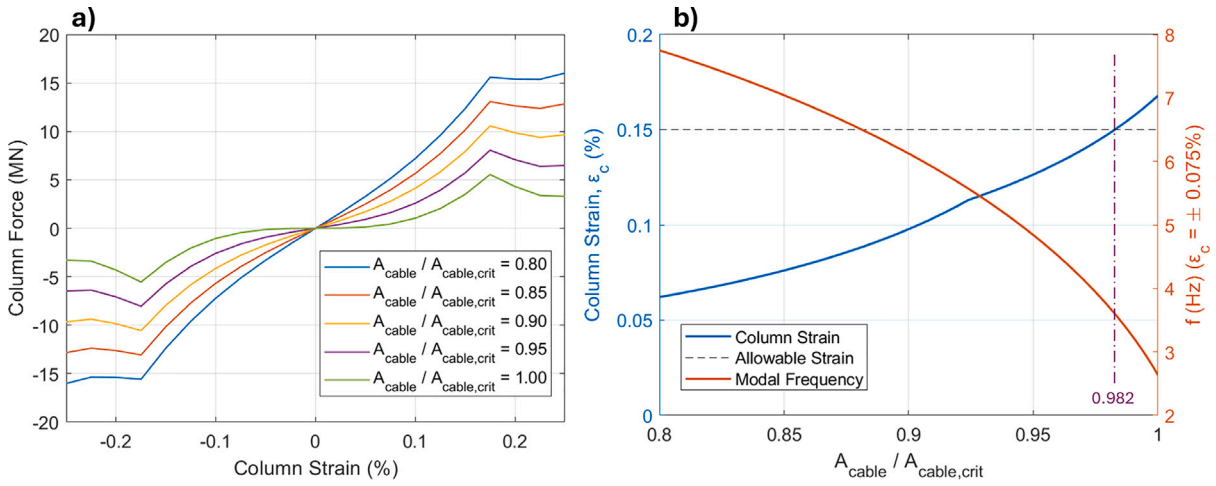

Fig. 12. (a) Nonlinear axial force-strain relationship for composite columns of SMR with NVIS device ($L_2 = L_3 = 0.15$ m, $L_4 = 0.4$ m, $l_4 = 0.1$ m, $\theta_3 = 3/8\pi$, σ_{init} = 800 MPa), and (b) effects of the $A_{cable}/A_{cable,crit}$ ratio of the NVIS device on the composite column axial strain and vertical coupled system frequency.

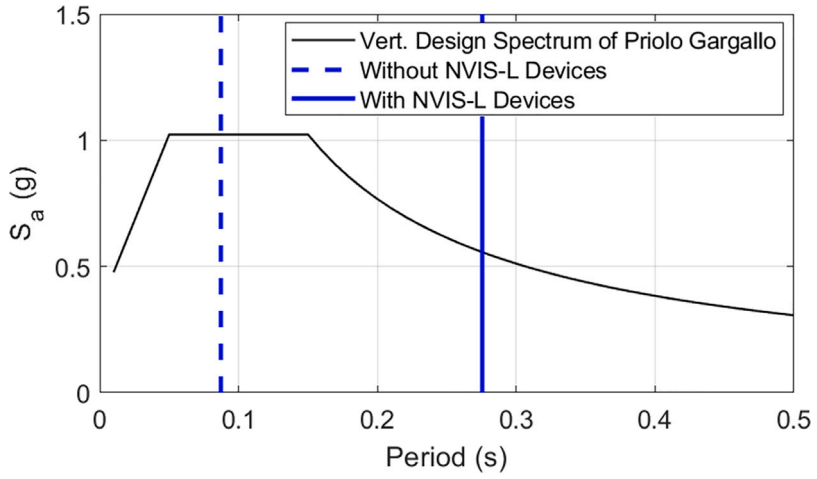

Fig. 13. Vertical Design spectrum of Priolo Gargallo with marked periods for the isolated and non-isolated SMR building.

To assess SMR standardisation, see [39], a site was chosen with seismic characteristics that exceeded the design level, i.e., beyond the design base earthquake (B-DBE). In this respect, it was assumed that the SMR plant was located in Priolo Gargallo, Sicily, Italy, with PGA_V = 0.36 g, corresponding to the 2% probability of exceedance in 50 years, exceeding the DBE level used for the standard SMR building design, i.e., PGA_V = 0.2 g. A set of eight recorded vertical components of natural ground motions was considered; the selection procedure was based on the matching between the mean spectrum and the mean spectrum plus one standard deviation of the selected accelerograms with the uniform hazard spectrum of Priolo Gargallo in a least-squares sense [45]. For clarity, Table 1 collects the details of the chosen ground motion records. For DBE, the selected ground motions were scaled down, specifically, the acceleration values of the original records for B-DBE were multiplied by a factor of 0.2g/0.36 g, where PGA_V = 0.2 g is the target DBE vertical peak acceleration.

The peak absolute vertical acceleration values of the SMR building are depicted in Fig. 14(a) for the main mass and Fig. 14(b) for the breathing mass of the pools. The data encompass results for both the DBE and B-DBE scenarios, along with their corresponding median values where vertical accelerations were reduced to 62%, clearly demonstrating the beneficial effects of the NVIS devices. For the DBE scenario, the selected ground motions were scaled down according to the ratio of PGAs. The inclusion of NVIS devices enables the safe installation of SMR buildings in seismically active zones that exceed standard

Table 1
Characteristics of the selected ground motion records.

No.	Event Name	Station	Rjb	Vs_{30}	M_w	PGA_V [g]
1	Erzincan, 1992	MM	13	421	6.6	0.25
2	S. Iceland, 2000	Kaldarholt	7	–	6.5	0.67
3	S. Iceland, 2000	Solheimar	11	–	6.4	0.42
4	L'Aquila, 2009	AQA	4.6	549	6.3	0.44
5	L'Aquila, 2009	AQG	4.4	696	6.3	0.24
6	L'Aquila, 2009	AQV	4.9	474	6.3	0.49
7	Landers, 1992	Joshua T.	11	379	7.3	0.18
8	Northridge-01, 1994	Castaic	20.1	450	6.7	0.22

design criteria, provided that horizontal protection is addressed. Fig. 15(a) depicts the acceleration histories for the sixth B-DBE ground motion, and the reduced acceleration of the main SMR mass is evident. Furthermore, Fig. 15(b) shows the peak column strain computed for each B-DBE ground motion. The observed strain levels remained well below the design limits, thereby confirming the feasibility of the proposed design approach. The higher column strains arose from a reduction in the effective vertical stiffness, which in turn led to increased deformations.

Beyond performance, constructability, inspection, and long-term maintenance are important for implementing NVIS in nuclear facilities. Seismic isolation experience in NPPs suggests designing for access

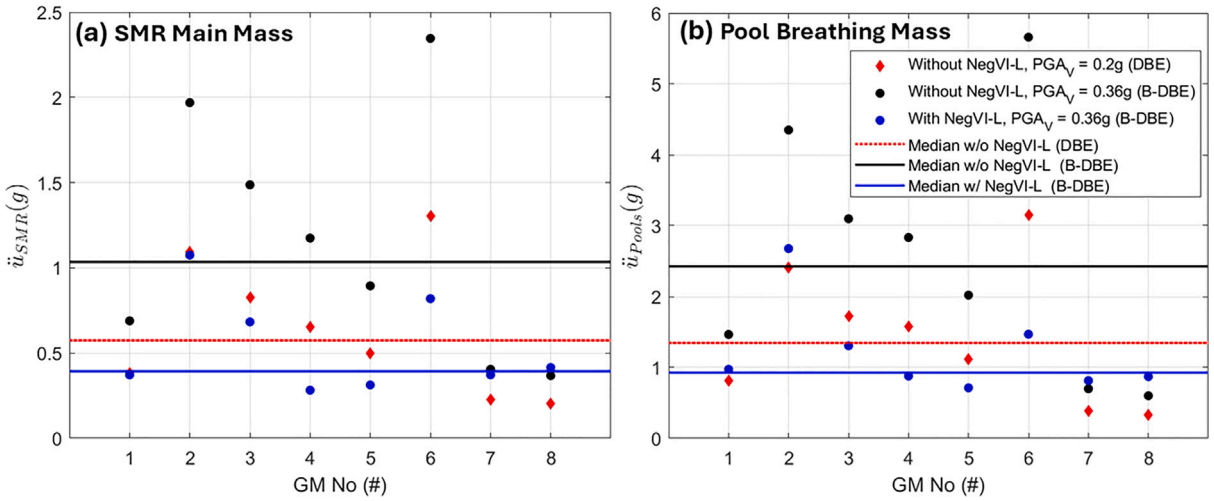

Fig. 14. Peak absolute vertical acceleration values for (a) the SMR main mass and (b) the pool breathing mass.

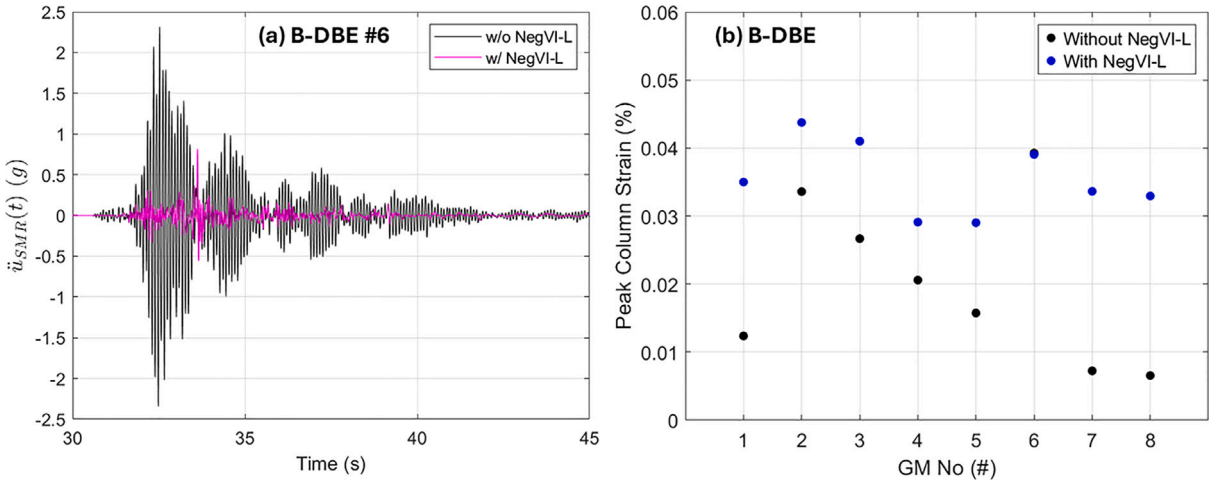

Fig. 15. (a) Acceleration histories of the SMR main mass for the sixth B-DBE ground motion; and (b) Maximum absolute strains on the composite columns of the SMR building subjected to B-DBE ground motions.

to allow periodic visual and functional checks [45]. NVIS devices generally require minimal maintenance, but scheduled inspections can detect issues such as corrosion, wear, or PT cable degradation. Attention to high-strength materials and their environmental interactions is essential for long-term reliability.

5. Three dimensional isolation of a pressurised spherical storage tank

The evaluation of NVIS devices was further conducted on a spherical liquid storage tank in combination with horizontal isolators. Spherical tanks are widely used in the petrochemical industry due to their uniform stress distribution and efficient storage of compressed gases such as LPG, propane, and propylene. However, during strong earthquakes, the supporting columns can bend, twist, or fail, potentially causing tank overturning, leaks, or explosions; a notable example occurred during the 2011 Tohoku earthquake in Tokyo Bay, Chiba [51]. Despite extensive research on storage tanks, few studies focus specifically on spherical tanks [52], and design codes have only recently begun to address them (e.g., second generation of Eurocode 8-4 [53]). Although Karamanos et al. [54] provided a simplified model for the horizontal linear sloshing in spherical tanks, a simplified model for vertical actions was not available. Thus, to model and capture the horizontal–vertical coupled sloshing of tank contents during seismic events, a FE analysis coupled with fluid–structure interactions was conducted using the Abaqus/Explicit [55] software and CEL approach was adopted.

5.1. Finite element modelling and details

The case study analysed was the one considered by Karamanos et al. [54], whose size is also consistent with the failed tanks in Tokyo Bay. The steel spherical tank has a diameter of 21.2 m with a wall thickness of 43 mm and contains propylene with a density of $\rho = 553\,\mathrm{kg/m^3}$. The tank is supported by 12 tubular steel columns and X-braces as depicted in Fig. 16. The FE model was based on Lagrangian S4R elements for both tank walls and columns, and connector elements were considered for braces. The problem of extreme element deformations in Lagrangian elements was addressed by simulating the fluid with Eulerian elements; thus, nonlinear sloshing effects were included. It should also be noted that for spherical liquid storage tanks under combined horizontal and vertical seismic excitation, fully coupled nonlinear sloshing and fluid–structure interaction must be considered; therefore, CEL analyses were employed for proper assessment. The horizontal rolling isolators were installed beneath the NVIS-equipped columns, so that the two systems operate in series: horizontal motions were mitigated through rolling isolators, while vertical loads were transmitted directly to NVIS due to the high vertical stiffness of the rolling

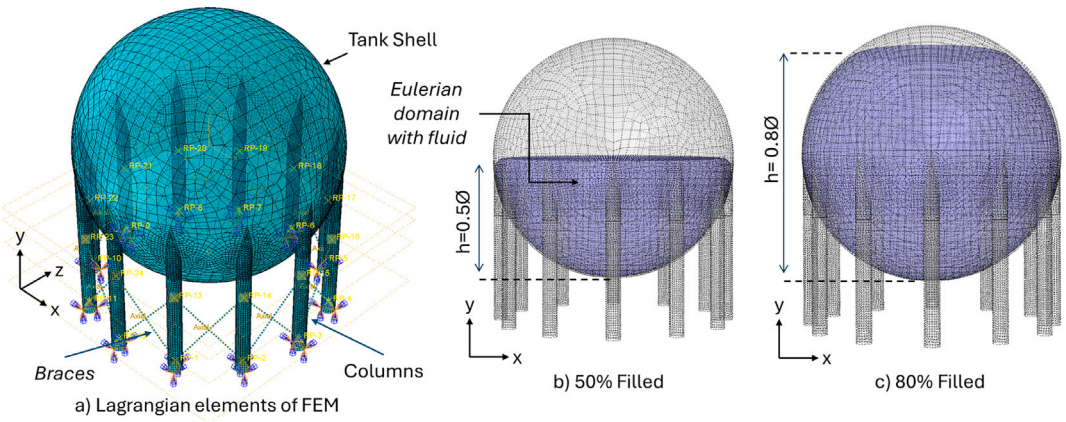

Fig. 16. FE model of the spherical tank after Karamanos et al. [54]: (a) Mesh details of Lagrangian elements and connectors; (b) Eulerian domain for the case with 50% filled tank; and (c) Eulerian domain for the case with 80% filled tank.

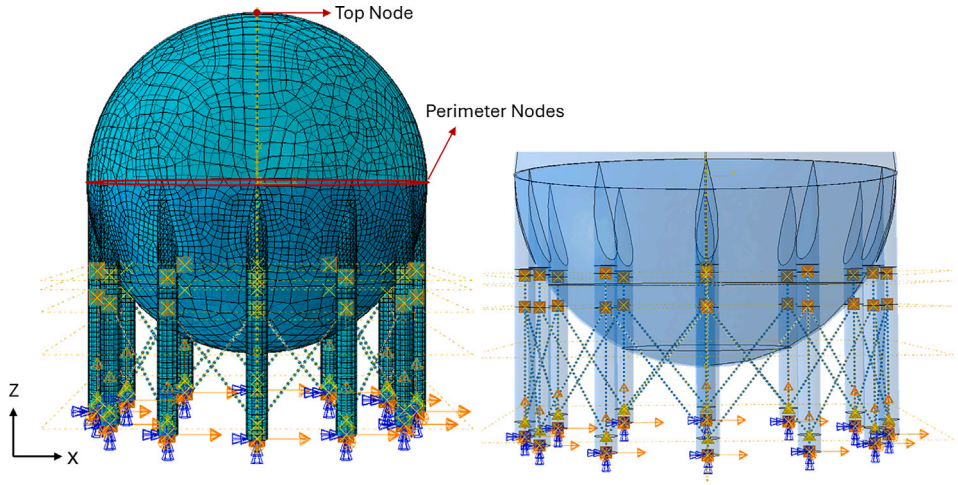

Fig. 17. FE model of the 3D isolated spherical tank with both rolling isolators and NVIS devices: (a) 3D FE mesh view; (b) links and reference points.

isolators. In addition, the hydrodynamic forces induced by sloshing were captured inherently by the fluid–structure interaction coupled and directly reflected in the predicted reaction and shear demands. To validate the modelling of fluid–structure interaction, the first horizontal convective periods of the 50% and 80% filled tanks were evaluated as $T_{C,50\%} = 5.4$ s and $T_{C,80\%} = 3.4$ s, respectively. These values are in close agreement with the results reported by Karamanos et al. [54] $T_{C,50\%} = 5.22$s and $T_{C,80\%} = 3.27$ s, confirming that the CEL model accurately captures the sloshing dynamics and providing confidence in the fidelity of the fluid–structure interaction simulation for the spherical tank case.

For the isolation of the spherical tank, NVIS devices were used in combination with rolling isolation devices, used in [56]. Consequently, the design isolation period for horizontal excitation was considered as $T_h = 2.5$ s, the isolators were located at the base of the column and assumed to be rigid in the vertical direction. Due to the effective length of the columns, that is 9.2 m, a high deformation in the columns can be sustained, then considering the NVIS devices with $H = 8$ m and $A_{cable}/A_{cable,crit} = 0.98$. The isolators were modelled using nonlinear connector elements. In view of the analysis, the displacement outputs were obtained both for the perimeter nodes and the top node of the tank, as highlighted in Fig. 17.

5.2. Time history analyses

To verify the performance of the NVIS devices, the isolated spherical tank was subjected to the GM record triplet of the 2011 Tohoku earthquake with ($M_W = 9.0$); these records were obtained from the CHB009 station, a station near the failed spherical tanks in Chiba, as indicated in Fig. 18(a). The triplet was characterised by $PGA_H = 0.24$ g and $PGA_V = 0.16$ g, respectively. The spectra of the triplet are also presented in Fig. 18.

The absolute maximum horizontal base shear and vertical base reaction values observed are reported in Table 2. Clear isolation benefits of NVIS device were observed for both 50% and 80% filled cases, highlighting 76% and 40% reduction in vertical base reactions, respectively. The observed reduction in horizontal base shear is due to the rolling isolation devices at the column bases, which increased the effective horizontal period of the system and thus limited the transmission of horizontal inertia forces to the tank. Moreover, Fig. 19 displays the comparison of the displacement histories of the top node of the 50% filled tank, together with the internal energy history E_I. In particular, E_I has been computed as,

$$E_I = E_E + E_P + E_{CD} \tag{24}$$

where E_E defines the recoverable elastic strain energy; E_P the energy dissipated through inelastic processes such as plasticity; E_{CD} the energy dissipated through viscoelasticity or creep. The energy dissipated by damping mechanisms and the external work of applied forces have been excluded from E_I. As expected, isolation results in higher displacements; however, an attentive reader can observe in Fig. 19(d) that the internal energy E_I of the tank remains limited. It should be highlighted that the reduction in vertical base reactions provided by the NVIS is accompanied by an increase in vertical displacement demand

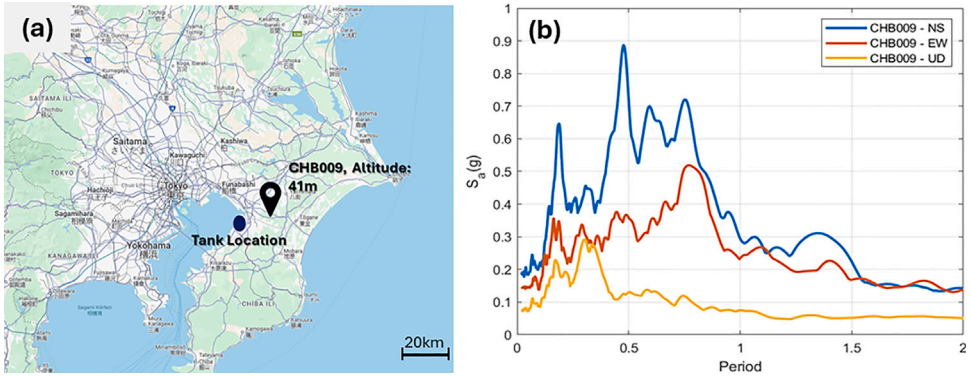

Fig. 18. (a) Location of the CHB009 station and its proximity to the spherical tank and (b) spectra of the 2011 Tohoku earthquake, CHB009 GM Triplet.

Table 2
Peak absolute horizontal and vertical base shear values.

	Base Shear X-dir.		Base Shear Y-dir.		Base Reaction Z-dir.	
Filling Ratio	50%	80%	50%	80%	50%	80%
Without Isolation (MN)	90.9	32.3	90.1	34	185.0	114
With Isolation (MN)	2.4	2.3	2.7	2.5	43.1	67.9

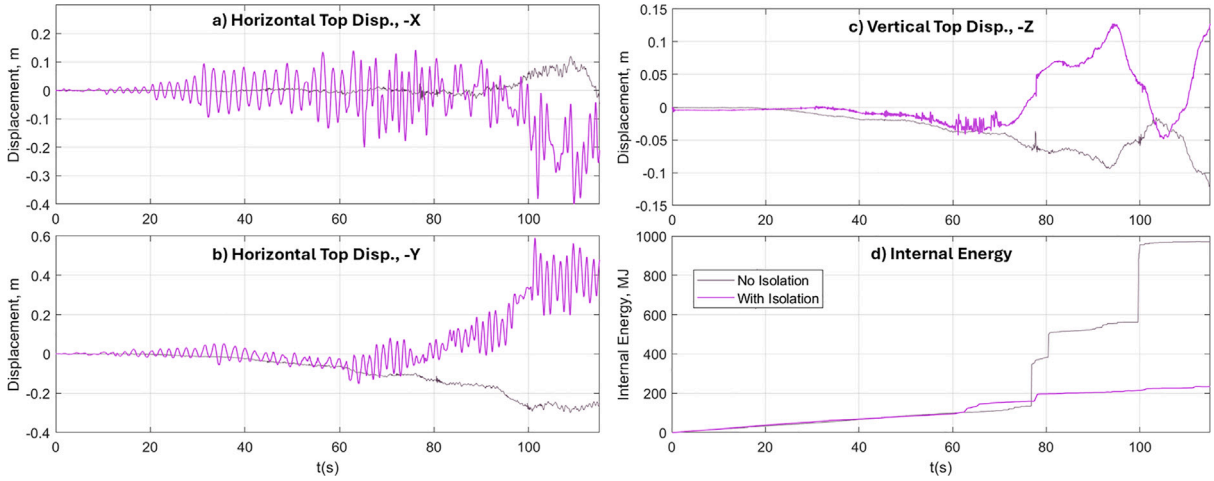

Fig. 19. (a-c) Displacement-time histories of the top nodes for the 50% filled spherical tank with and without isolation; (d) time history of the internal energy E_I.

at the isolation level. Therefore, practical implementation requires sufficient clearance and appropriate detailing of piping systems and other connected auxiliary components to accommodate the expected isolation stroke, ensuring that contact, damage, or serviceability issues do not arise during strong seismic events.

Moreover, when 3D isolation solutions were introduced, a critical issue underlined by researchers was the control of rocking and torsional motions [57]. To evaluate these issues, the peak displacement variations at the perimeter nodes were calculated and are reported in Fig. 20. More precisely, whilst the variations in the X and Y directions correspond to torsional motions, the variation in vertical displacements, see Fig. 20(c), corresponds to rocking motions. For rocking, the maximum variation was observed at $t = 100.55$ s with $\Delta u = 0.047$ mm. Considering that the tank retains its circular shape, the aforementioned displacement value corresponds to $\theta_r = 0.022$ rad, i.e., a rather small rocking motion. This result was expected as the proposed NVIS mechanism is endowed with a hardening force–displacement behaviour. Clearly, as the displacement increases, the equivalent vertical stiffness increases with a cubic relationship, as shown in Fig. 4. This favourable behaviour prevents excessive displacements and, thus, rocking motions. Finally, the peak torsional motion was observed at $t = 62.6$ s and was calculated to read $\theta_t = 0.009$ rad.

6. Conclusions

This study has introduced Negative-Stiffness Based Vertical ISolator (NVIS) as an innovative approach to mitigate vertical seismic hazards in process and power plant structures. By integrating PT cables with mechanisms, NVIS overcomes common issues, such as buckling in conventional compression-based approaches, whilst providing a lightweight, straightforward, and tunable alternative. A notable advantage of the NVIS system was represented by the retrofit capabilities, which can be accomplished without cutting existing columns and only requiring minimal modifications, addressing a persistent challenge in structural retrofitting.

Through static and dynamic analyses supported by experimental validation and comprehensive case studies, the performance of the NVIS device was demonstrated. The investigations confirmed that friction within the connection interfaces of the components does not significantly affect dynamic performance. Experimental observations

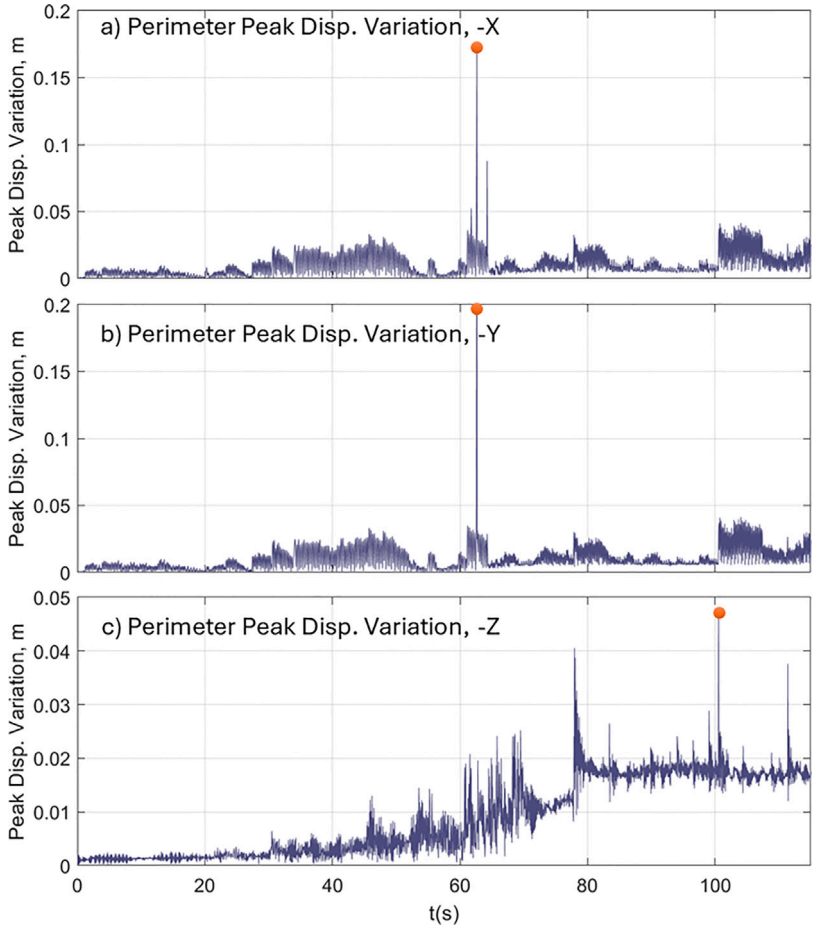

Fig. 20. Peak displacement variations at the perimeter nodes of the isolated spherical tank 50% filled.

indicate that while NVIS devices perform effectively, practical challenges such as ensuring precise assembly tolerances, local deformations, maintaining cable tension over time, and addressing wear or friction effects must be carefully managed for reliable long-term operation in large-scale industrial applications.

In a case study involving a Small Modular Reactor (SMR) building, NVIS devices not only provided vertical seismic protection, reducing vertical accelerations by 62%, but also ensured that the standardised SMR building could be safely built at locations with hazard spectra beyond the design spectrum. Furthermore, when NVIS were evaluated in combination with conventional horizontal isolators, such as the case of a spherical liquid storage tank, the NVIS devices reduced the vertical peak base reactions by about 76% and 40% for 50% and 80% of the filled tank cases, whilst effectively limiting rocking due to their hardening nonlinearity. Overall, the proposed research work has provided an understanding of the behaviour, performance, design, and practical implementation of the proposed devices, paving the way for their broader application in seismic protection strategies.

The results directly address the original objectives of developing a scalable, tunable, and retrofit-capable NVIS for vertical seismic isolation. Analyses, experimental validation, and case studies confirm that the system achieves effective vertical isolation, maintains structural stability in compliance with regulatory requirements, and provides a practical solution for both new and existing industrial structures. These findings demonstrate that the NVIS fulfils its intended purpose, bridging gaps in current vertical isolation technologies and validating the proposed approach.

NVIS devices provide the greatest benefit in scenarios where vertical seismic hazards are significant, such as critical infrastructure, heavy machinery or equipment in process and power plants, and structures with low natural vertical damping. They can be applied either by retrofitting existing horizontally isolated structures that require vertical protection or in new constructions in combination with horizontal isolation solutions. As highlighted in Section 4, standardised structures such as SMR buildings stand to gain the most, particularly when planned at sites where vertical hazard levels exceed the design spectrum. Nevertheless, NVIS applicability can be limited for structures with short columns, lightweight structures and buildings or structures with low vertical seismic demand, where the benefits may be marginal. Practical constraints such as available space, constructability, and maintenance access should also be considered when selecting NVIS for a particular application.

Building on the design and application of NVISs devices, future advances can include: (i) experimental validation through large-scale shake table tests to further confirm their efficacy and refine their design; (ii) exploration of high-damping components or advanced metamaterials with low compliance to further enhance isolator performance; (iii) studies to consider their long-term behaviour under multi-hazard conditions and environmental variability; (iv) the potential influence of second-order (P–Δ) effects under extreme combined vertical and horizontal seismic excitations; and (v) assessment of challenges related to the adoption, including the effect of truss and mechanism flexibility at large scale, durability and fatigue life of PT cables, maintenance requirements, reliability over extended service periods, and compliance with industrial certification and safety standards. Addressing these aspects will provide critical guidance for practical implementation of NVIS in real-world industrial facilities.

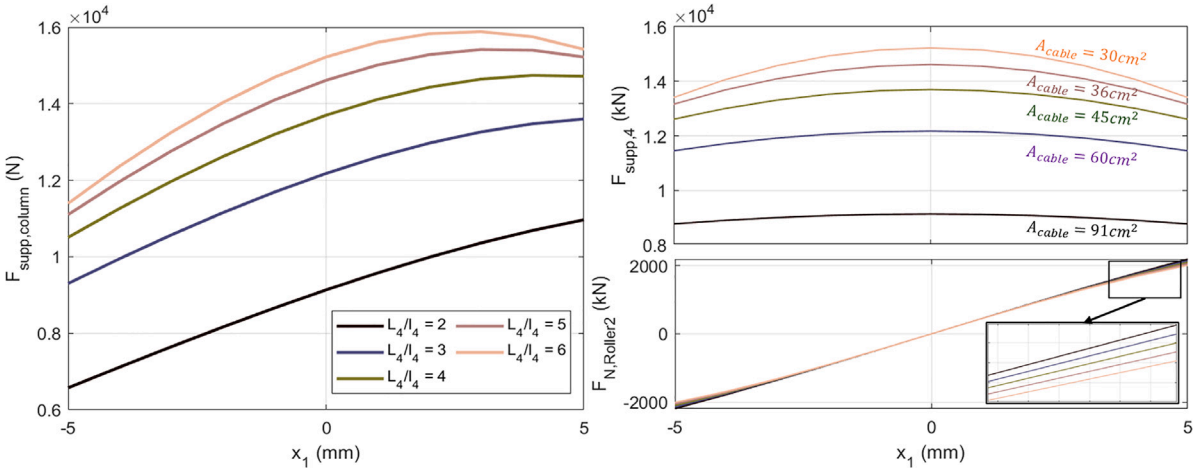

Fig. A.21. (a) Axial Load on the support column of the NVIS device for various L_4/l_4 values; (b) load on the support #4; (c) vertical load on the Roller #2.

CRediT authorship contribution statement

T. Guner: Writing – original draft, Software, Methodology, Formal analysis, Conceptualization. **O.S. Bursi:** Writing – review & editing, Supervision, Resources, Methodology.

Financial disclosure

None reported.

Declaration of competing interest

The authors declare that they have no known competing financial interests or personal relationships that could have appeared to influence the work reported in this paper.

Acknowledgements

All authors acknowledge the Italian Ministry of Education, Universities, and Research (MUR), Italy in the framework of the project DICAM-EXC (Departments of Excellence 2023–2027, grant L232/2016).

Appendix. Axial loads on support columns of nvis devices

From force equilibrium, each support column of the NVIS device needs to carry the governing load of the PT cable and the resultant force when $x_1 \neq 0$, i.e.

$$F_{supp,column} \gg F_{supp,4} + \frac{P_2 x_1}{L_2} \tag{A.1}$$

where $\frac{P_2 x_1}{L_2} = F_{N,roller,2}$, i.e. the vertical load on the Roller #2, whilst $F_{supp,4}$ reads:

$$F_{supp,4} = k_{cable}\left(L_{cable}\varepsilon_{init} + x_3 L_4/l_4\right)(L_4/l_4 - 1) \tag{A.2}$$

It is worth pointing out that the use of the amplifier mechanism between the cable and the support point #4, see Fig. 3, reduces the required force on the cable and reduces the stress on the support column. The loads on the support structure for various L_4/l_4 values are provided in Fig. A.21, including the distribution of the axial load between supports. Clearly, the selection of the lever arm ratio L_4/l_4 is critical, both for optimum performance and for optimum dimensions of the support structure, directly affecting costs.

Data availability

Data will be made available on request.

References

[1] Politopoulos I, Moussallam N. Horizontal floor response spectra of base-isolated buildings due to vertical excitation. Earthq Eng Struct Dyn 2012;41(3):587–92.
[2] Papazoglou A, Elnashai A. Analytical and field evidence of the damaging effect of vertical earthquake ground motion. Earthq Eng Struct Dyn 1996;25(10):1109–37.
[3] Ambraseys Nu, Simpson K. Prediction of vertical response spectra in Europe. Earthq Eng Struct Dyn 1996;25(4):401–12.
[4] Sagbas G, Sheikhi Garjan R, Sarikaya K, Deniz D. Field reconnaissance on seismic performance and functionality of Turkish industrial facilities affected by the 2023 Kahramanmaras earthquake sequence. Bull Earthq Eng 2024;22(1):227–54.
[5] Zhou Z, Wong J, Mahin S. Potentiality of using vertical and three-dimensional isolation systems in nuclear structures. Nucl Eng Technol 2016;48(5):1237–51.
[6] Hosseini SEA, Beskhyroun S. Fluid storage tanks: A review on dynamic behaviour modelling, seismic energy-dissipating devices, structural control, and structural health monitoring techniques. In: Structures, vol. 49, Elsevier; 2023, p. 537–56.
[7] Kunnath SK, Erduran E, Chai Y, Yashinsky M. Effect of near-fault vertical ground motions on seismic response of highway overcrossings. J Bridg Eng 2008;13(3):282–90.
[8] Iemura H, Pradono MH. Advances in the development of pseudo-negative-stiffness dampers for seismic response control. Struct Control Health Monit: Off J Int Assoc Struct Control Monit Eur Assoc Control Struct 2009;16(7–8):784–99.
[9] Sarlis A, Pasala D, Constantinou MC, Reinhorn AM, Nagarajaiah S, Taylor DP. Negative stiffness device for seismic protection of structures: shake table testing of a seismically isolated structure. J Struct Eng 2016;142(5):04016005.
[10] Li H, Bi K, Han Q, Ma R. A state-of-the-art review on negative stiffness-based structural vibration control. Eng Struct 2025;323:119247.
[11] Li H, Li Y, Li J. Negative stiffness devices for vibration isolation applications: a review. Adv Struct Eng 2020;23(8):1739–55.
[12] Le TD, Ahn KK. A vibration isolation system in low frequency excitation region using negative stiffness structure for vehicle seat. J Sound Vib 2011;330(26):6311–35.
[13] Palomares E, Nieto A, Morales A, Chicharro J, Pintado P. Numerical and experimental analysis of a vibration isolator equipped with a negative stiffness system. J Sound Vib 2018;414:31–42.
[14] Chen P, Wang B, Dai K, Li T. Analytical and numerical investigations of base isolation system with negative stiffness devices. Eng Struct 2022;268:114799.
[15] Chen X, Ikago K, Guan Z, Li J, Wang X. Lead-rubber-bearing with negative stiffness springs (LRB-NS) for base-isolation seismic design of resilient bridges: A theoretical feasibility study. Eng Struct 2022;266:114601.
[16] Kapasakalis KA, Antoniadis IA, Sapountzakis EJ. Constrained optimal design of seismic base absorbers based on an extended KDamper concept. Eng Struct 2021;226:111312.
[17] Kalogerakou ME, Kapasakalis KA, Antoniadis IA, Sapountzakis EJ. Vertical seismic protection of structures with inerter-based negative stiffness absorbers. Bull Earthq Eng 2022;1–42.
[18] Liu C, Zhang W, Yu K, Liu T, Zheng Y. Quasi-zero-stiffness vibration isolation: designs, improvements and applications. Eng Struct 2024;301:117282.

[19] Aiken ID, Kelly JM, Tajirian FF. Mechanics of low shape factor elastomeric seismic isolation bearings. Earthquake Engineering Research Center, College of Engineering, University . . . ; 1989.
[20] Nielsen G, Rees S, Zekioglu A, Sarebanha A, Biscombe L, Shao B, Dong B. A 3-d seismic isolation system to protect the loma linda university hospital from near-fault earthquakes. In: Proceedings of 17th world conference on earthquake engineering. 2022, p. 1.
[21] Inoue K, Fushimi M, Moro S, Morishita M, Kitamura S, Fujita T. Development of three-dimensional seismic isolation system for next generation nuclear power plant. In: Proceedings of the 13th world conference on earthquake engineering. vancouver, BC, Canada; 2004, p. 1–6.
[22] Miyagawa T, Watakabe T, Yamamoto T, Fukasawa T, Okamura S. Research and development of three dimensional seismic isolation system utilized coned-disc-springs with rubber bearings. In: Pressure vessels and piping conference, vol. 58035, American Society of Mechanical Engineers; 2017, V008T08A043.
[23] Cimellaro GP, Domaneschi M, Warn G. Three-dimensional base isolation using vertical negative stiffness devices. J Earthq Eng 2020;24(12):2004–32.
[24] Dong Z-Q, Li C, Li G, Yu D-H, Sun B-L, Liu L-K. Analysis and experiment of a novel three-directional vibration isolator with variable damping and stiffness. Mech Syst Signal Process 2025;238:113179.
[25] Najafijozani M, Becker TC, Konstantinidis D. Evaluating adaptive vertical seismic isolation for equipment in nuclear power plants. Nucl Eng Des 2020;358:110399.
[26] Warn GP, Whittaker AS. A Study of the Coupled Horizontal-Vertical Behavior of Elastomeric and Lead-Rubber Seismic Isolation Bearings. Tech. Rep. MCEER-06-0011, Multidisciplinary Center for Earthquake Engineering Research; 2006.
[27] Xu H, He W, Zhang L, Liu W. Shaking table test of a novel Three-dimensional seismic isolation system with inclined rubber bearings. Eng Struct 2023;293:116609.
[28] Han Q, Jing M, Lu Y, Liu M. Mechanical behaviors of air spring-FPS three-dimensional isolation bearing and isolation performance analysis. Soil Dyn Earthq Eng 2021;149:106872.
[29] Mo Z, Shu G, Lai B, Yang T, Ventura CE. Experiment and analysis of air spring vertical seismic isolation device. In: Structures, vol. 66, Elsevier; 2024, 106869.
[30] Araki Y, Asai T, Masui T. Vertical vibration isolator having piecewise-constant restoring force. Earthq Eng Struct Dyn 2009;38(13):1505–23.
[31] Okamura S, Kitamura S, Takahashi K, Somaki T. Experimental study on vertical component isolation system. In: Proceedings of the 18th international conference on structural mechanics in reactor technology. Beijing: Atomic Energy Press; 2005, p. 3411–22.
[32] Wang W, Wang X. Tests, model, and applications for coned-disc-spring vertical isolation bearings. Bull Earthq Eng 2020;18:357–98.
[33] Tomizawa T, Takahashi O, Aida H, Suhara J, Saruta M, Okada K, Tsuyuki Y, Suzuki T, Fujita T. Vibration test in a building named ‘chisuikan’using three-dimensional seismic isolation system. In: Proc., 15th world conf. on earthquake engineering. Lisboa, Portugal: Portuguese society for earthquake engineering; 2012, p. 1.
[34] Chen Z, Ding Y, Shi Y, Li Z. A vertical isolation device with variable stiffness for long-span spatial structures. Soil Dyn Earthq Eng 2019;123:543–58.
[35] Zhu X, Lin G, Pan R, Li J. Design and analysis of isolation effectiveness for three-dimensional base-seismic isolation of nuclear island building. Nucl Eng Technol 2022;54(1):374–85.
[36] Liu Y, Li J, Lin G. Seismic performance of advanced three-dimensional base-isolated nuclear structures in complex-layered sites. Eng Struct 2023;289:116247.
[37] American Society of Civil Engineers. Minimum design loads and associated criteria for buildings and other structures. Reston, VA: American Society of Civil Engineers; 2017, ASCE/SEI 7-16 Edition. Standard ASCE/SEI 7-16.
[38] European Committee for Standardization. Anti-seismic devices. 2018, European Standard, UNI EN 15129:2018.
[39] Guner T, Nardin C, Bursi OS, Erlicher S, Monteil A. Design standardisation and seismic protection of SMRs through modular metafoundations. Nucl Eng Des 2024;426:113347.
[40] The MathWorks, Inc. MATLAB: The language of technical computing. Natick, Massachusetts, United States: The MathWorks, Inc. 2023, URL https://www.mathworks.com. Version R2023a.
[41] Parsi SS, Lal KM, Kosbab BD, Ingersoll ED, Shirvan K, Whittaker AS. Seismic isolation: A pathway to standardized advanced nuclear reactors. Nucl Eng Des 2022;387:111445.
[42] International Atomic Energy Agency. Design safety considerations for water cooled small modular reactors incorporating lessons learned from the fukushima daiichi accident. Tech. Rep. IAEA-TECDOC-1785, Vienna, Austria: IAEA; 2016.
[43] Lloyd CA, Roulstone T, Lyons RE. Transport, constructability, and economic advantages of SMR modularization. Prog Nucl Energy 2021;134:103672.
[44] Power N. VOYGR SMR plants. 2025, URL https://www.nuscalepower.com/en/products/voygr-smr-plants. [Accessed 12 March 2025].
[45] Guner T, Bursi OS, Erlicher S. Optimization and performance of metafoundations for seismic isolation of small modular reactors. Comput-Aided Civ Infrastruct Eng 2023;38(12):1558–82.
[46] European Committee for Standardization. Eurocode 4: Design of composite steel and concrete structures – Part 2: General rules and rules for bridges. Brussels: European Committee for Standardization; 2005, Eurocode 4 – EN 1994-2:2005.
[47] European Committee for Standardization. Eurocode 3: Design of steel structures – Part 1-1: General rules and rules for buildings. EN 1993-1-1, Brussels: European Committee for Standardization; 2005, Eurocode 3 – EN 1993-1-1:2005.
[48] European Committee for Standardization. Eurocode 4: Design of composite steel and concrete structures – Part 1-1: General rules and rules for buildings. EN 1994-1-1, Brussels: European Committee for Standardization; 2004, Eurocode 4 – EN 1994-1-1:2004.
[49] European Committee for Standardization. Eurocode 8: Design of structures for earthquake resistance – Part 1: General rules, seismic actions and rules for buildings. In: EN 1998-1, Brussels: European Committee for Standardization; 2004, Eurocode 8 – EN 1998-1:2004.
[50] Chopra AK. Dynamics of Structures. 5th ed. Pearson; 2017.
[51] Li X, Koseki H, Mannan MS. Case study: Assessment on large scale LPG BLEVEs in the 2011 Tohoku earthquakes. J Loss Prev Process Ind 2015;35:257–66.
[52] Lü Y, Sun J, Sun Z, Cui L, Wang Z. Basic theory of simplified dynamic model for spherical tank considering swinging effect. J Press Vessel Technol 2019;141(6):061202.
[53] European Committee for Standardization. Eurocode 8: Design of structures for earthquake resistance – Part 4: Silos, tanks and pipelines. EN 1998-4, Brussels: European Committee for Standardization; 2006, Eurocode 8 – EN 1998-4:2006.
[54] Karamanos SA, Patkas LA, Platyrrachos MA. Sloshing effects on the seismic design of horizontal-cylindrical and spherical industrial vessels. J Press Vessel Technol 2005;128(3):328–40. http://dx.doi.org/10.1115/1.2217965.
[55] Dassault Systèmes Simulia Corp. Abaqus/explicit user’s manual. 2025, URL https://www.3ds.com/products-services/simulia/products/abaqus/. [Accessed 12 March 2025].
[56] Lyu Y, Sun J, Li Z, Teng J, Cui L, Cheng L. Study on mechanical model and shaking table test of spherical tank rolling isolation. Earthq Eng Struct Dyn 2022;51(8):1895–917.
[57] Medel-Vera C, Ji T. Seismic protection technology for nuclear power plants: a systematic review. J Nucl Sci Technol 2015;52(5):607–32.